

UC Irvine

UC Irvine Electronic Theses and Dissertations

Title

Nanoscale IR Spectroscopy Based on Molecular Optomechanical Damping

Permalink

<https://escholarship.org/uc/item/81d385vw>

Author

Almajhadi, Mohammad A.

Publication Date

2021

Peer reviewed|Thesis/dissertation

UNIVERSITY OF CALIFORNIA,
IRVINE

Nanoscale IR Spectroscopy Based on Molecular Optomechanical Damping

DISSERTATION

submitted in partial satisfaction of the requirements
for the degree of

DOCTOR OF PHILOSOPHY

in Electrical Engineering and Computer Science

by

Mohammad A. Almajhadi

Dissertation Committee:
Professor H. Kumar Wickramasinghe, Chair
Professor Peter Burke
Professor Ozdal Boyraz

2021

Chapter 2.3 © Optical Express
Chapter 2.4 © Nature Communication
All other materials © 2021 Mohammad A. Almajhadi

DEDICATION

This work is dedicated to my mother may she rest in peace,
to the first-generation PhD students,
and to those who were not lucky to have supportive advisor

TABLE OF CONTENTS

DEDICATION	ii
TABLE OF CONTENTS	iii
LIST OF FIGURES.....	v
LIST OF TABLES.....	ix
ACKNOWLEDGEMENTS	x
VITA	xi
ABSTRACT OF THE DISSERTATION.....	xiii
1 Amplitude modulation atomic force microscopy.....	1
1.1 Introduction	1
1.2 Tip-sample van der Waals interactions (sphere-plane model)	4
1.3 Tip-sample conservative and dissipative interactions	8
2 Photoinduced force microscopy.....	15
2.1 Introduction:	15
2.2 The debate.....	19
2.3 Contrast and imaging performance in photo induced force microscopy.....	23
2.3.1 Introduction.....	23
2.3.2 Brief theory of near field optical forces in PiFM	24
2.3.3 Problem setup	26
2.3.4 Bench marking against known closed form expression	28

2.3.5	Effect of coating materials and thickness.....	29
2.3.6	Optical force spectrum at an absorption band	32
2.3.7	Lateral, subsurface, and spectral imaging performance	34
2.3.8	Discussion	38
2.3.9	Conclusion.....	39
2.4	Nanoscale Opto-Mechanical Molecular Damping as the Origin of Spectroscopic Contrast in Photo Induced Force Microscopy	41
2.4.1	Introduction:.....	41
2.4.2	Distinguishing Between Repulsive and Attractive Optical Forces.....	44
2.4.3	Piezo Vibration Experiments and PiFM Sensitivity to Thermal Expansion.	47
2.4.4	Monolayer PiFM Experiments.....	49
2.4.5	Opto-mechanical damping.....	51
2.4.6	Discussion	57
	References.....	59

LIST OF FIGURES

Fig. 1 Atomic force microscopy apparatus (A). Close look to the tip-sample junction (B).
 Force-distance curve extracted using contact mode AFM (C). 4

Fig. 2 Conservative and dissipative tip-sample interactions (A) and (D). The change in
 the oscillation amplitude due to conservative (B) and dissipative (E) interactions.
 The change in the oscillation phase due to conservative (C) and dissipative (F)
 interactions. 11

Fig. 3 The configuration set up. Tip, with 10° half taper angle, is terminated by spherical
 section of 100 \AA radius. In (a), the tip is coated by metal with different coating
 thicknesses (T_{th}), and the Si substrate (not shown) is coated by a sample with
 different sample coating thicknesses (S_{th}). The amplitude of the electric field is
 calculated along a - - a' and b - - b' line segments. In (b), a particle 50 \AA radius is
 placed at a depth d within the sample. Arrows 1 and 2 indicate the sweeping
 direction of the particle. Tip-sample distance is 5 \AA . The geometry is irradiated by
 standing wave with polarization parallel to the tip axis..... 27

Fig. 4 MST and pressure force (PF) calculated by COMSOL, and PF calculated by Mie
 equations. 29

Fig. 5 Gap-field enhancement (E_{enh}) (left column) and $\langle F_{opt} \rangle$ (right column) as a function
 of T_{th} , where each curve represents specific S_{th} . (a), (b), and (c) correspond to
 different tip-coating materials: platinum (Pt), silver (Ag), and gold (Au). The incident
 wavelength is $10 \mu\text{m}$ 31

Fig. 6 (a) Near-field distribution is calculated at $T_{th} = 5 \text{ nm}$. The spatial confinement of
 the electric field calculated through a - - a' segment (b) and vertically through b - - b'

segment (c) (cf. Fig. 3(a)). Each color represents different T_{th} . S_{th} is 30 nm and the tip-coating material is Au. 32

Fig. 7(a) $\langle F_{opt} \rangle$ as a function of PMMA absorption band (left) and the real (α') and imaginary (α'') parts of PMMA polarizability (right). (b) $\langle F_{opt} \rangle$ as a function of PS absorption band (left), and α' and α'' parts of PS polarizability (right). (c) $\langle F_{opt} \rangle$ calculated in the visible region for Au (left), and α' and α'' parts of Au polarizability (right); the bulk Au polarizability is drawn in solid, and nanoparticle Au polarizability is drawn in dashed line. 34

Fig. 8 (a) and (b) are the $\langle F_{opt} \rangle$ calculated as a function of particle depth d (direction 2 (cf. Fig. 1(b))). (c) and (d) are $\langle F_{cont} \rangle$ calculated while the particle is swept in direction 1 for different depths d . The particles are excited at resonance. 36

Fig. 9 F_{cont} at on optical resonance (solid red line) and off optical resonance (dashed red line) conditions for Au (a), PS (b), SiC (c). 38

Fig. 10 Schematic of IR PiFM experiment and principle of opto-mechanical damping. a The cantilever is mechanically vibrated at its 2nd mechanical eigenmode f_2 , so that peak-peak oscillation is 6 nm. Lock-in amplifier and feedback laser position sensitive detector (PSD) are used to stabilize the cantilever nanometers from sample surface. The IR source is electrically triggered at $f_m = f_2 - f_1$, where f_1 is the 1st mechanical eigenmode of the cantilever. The incident infrared pulse is p-polarized (along the tip axis) and focused to 20-um-diameter spot. The topography and the PiFM signals are simultaneously recorded at f_2 and f_1 respectively. The image is generated via raster-scanning the sample under the tip. b illustrates the

principle of opto-mechanical damping, where oscillation amplitude is damped due to IR vibrational resonance.....	43
Fig. 11 Cantilever frequency shift across an absorption band. Shift of the cantilever resonance frequency at f_1 (blue line) across PS absorption band at 1495 cm^{-1} (Orange line). The sample is 60 nm thick PS film on Au substrate. Input average power was 1 mW focused to 20-um-diameter spot.....	45
Fig. 12 Measurement of gas photo-acoustic waves while tip is retracted from sample by $3\text{ }\mu\text{m}$. a 500 nm thick PMMA was excited by infrared laser source modulated at $f_m = f_1$ (direct PiFM mode), where tip-sample distance is about $3\text{ }\mu\text{m}$. The tip-sample system were enclosed in a vacuum chamber and an air pump is used to decrease pressure. b-d Photoacoustic signals at 1.7 Torr, 0.5 Torr, and 0.3 Torr respectively	46
Fig. 13 Interferometric setup for calibrating the PZT Crystal.	47
Fig. 14 Non-contact AFM sensitivity to thermal expansion. a The peak-peak oscillation amplitude (blue solid line) measured at f_1 as a function of the PZT displacement amplitude (d). The noise level of the system measured at f_1 corresponds to oscillation of about 50 pm peak-peak as indicated by the orange line. Tip-sample gap is controlled at f_2 and the PZT is driven at $f_m = f_2 - f_1$. b depicts the experimental setup.....	49
Fig. 15 Monolayer response. a is 4-MBT adsorbed on template-stripped gold. Excitation average power is 0.5 mW focused to 20-um-diameter spot. b is point spectrum of 4-MBT showing resonance at 1495 cm^{-1} . c – e are topography of gold island, PiFM image at 1495 cm^{-1} , and PiFM image off resonance respectively.....	51

Fig. 16 Phase measurement comparison between left and right excitation. Amplitude change of the 2nd mechanical mode due to conservative a and dissipative b interactions. The expected relative phase between f_{2R} (a-a') and f_{2L} (b-b') excitations, measured at the 1st mechanical mode is shown in c and d. Phase measurement of the 1st mechanical mode for left excitation e and right excitation f. The phase and amplitude are measured using lock-in amplifier. 53

Fig. 17 1st and 2nd mechanical modes of the cantilever used in this paper. Note that at 1 MHz there is no cantilever oscillation, and $f_2 - f_m$ does not overlap with f_1 54

Fig. 18 Opto-mechanical damping. a and b are phase and amplitude of high Q (red) and low Q (black) harmonic oscillator. Change in the phase (φ_2) and amplitude (A_2) of the 2nd mechanical mode (blue line) across PMMA absorption band (orange line) centered at 1733 cm^{-1} for right excitation c and d and left excitation e and f. Sample is 60 nm thick PMMA on glass. The phase measurements were conducted using standard PiFM mixing mode, while amplitude measurements were conducted with the feedback loop open and the wavenumber scanned rapidly through resonance as explained in the text. 56

LIST OF TABLES

Table 1: Dielectric functions used to find $\langle F_{\text{cont}} \rangle$ for ON and OFF resonance..... 37

ACKNOWLEDGEMENTS

Working with nanoimaging technology such as photoinduced force microscopy (PiFM) was full of challenges. However, the challenges became opportunities to further enhance our understanding about light-matter interactions in nanoscale dimensions.

The 5 years that I spent were a scientific journey that I am proud of. I would like to thank my committee chair, Professor H. Kumar Wickramasinghe for the insightful suggestions and discussions.

I would like to thank my committee members Professor Peter Burke and Professor Ozdal Boyraz for reviewing my thesis and for their advises and comments. Special thanks to Derek Nowak for the experimental training and the insightful comments, and to Tom Albrecht and Sung Park for the insightful discussions.

VITA

Mohammad A. Almajhadi

- 2011 Bachelor of Science in Electrical Engineering
University of Hail
- 2012-2013 Teaching Assistant
University of Hail
- 2016 Master of science in Electrical Engineering and Computer Science
University of California, Irvine
- 2021 Ph.D. in Electrical Engineering and Computer Science
University of California, Irvine

LIST OF PUBLICATIONS

1. **Almajhadi, M.** & Wickramasinghe, H. K. Contrast and imaging performance in photo induced force microscopy. *Opt. Express*, OE 25, 26923–26938 (2017).
2. Huang, F., Tamma, V. A., Rajaei, M., **Almajhadi, M.** & Kumar Wickramasinghe, H. Measurement of laterally induced optical forces at the nanoscale. *Appl. Phys. Lett.* 110, 063103 (2017).
3. Rajaei, M., **Almajhadi, M. A.**, Zeng, J. & Wickramasinghe, H. K. Near-field nanoprobng using Si tip-Au nanoparticle photoinduced force microscopy with 120:1 signal-to-noise ratio, sub-6-nm resolution. *Opt. Express*, OE 26, 26365–26376 (2018).

4. **Almajhadi, M. A.**, Uddin, S. M. A. & Wickramasinghe, H. K. Observation of nanoscale opto-mechanical molecular damping as the origin of spectroscopic contrast in photo induced force microscopy. *Nat Commun* 11, 5691 (2020).
5. **Almajhadi, M. A.**, Uddin, S. M. A. & Wickramasinghe, H. K. Observation of Nanoscale Opto-Mechanical Molecular Damping; Origin of Spectroscopic Contrast in Infrared Photo Induced Force Microscopy. in 2020 Conference on Lasers and Electro-Optics (CLEO) 1–2 (2020).
6. Chávez-Madero, C. et al. Using chaotic advection for facile high-throughput fabrication of ordered multilayer micro- and nanostructures: continuous chaotic printing. *Biofabrication* 12, 035023 (2020).
7. Holmberg, S., Norma Alicia Garza-Flores, **Almajhadi, M. A.** et al. Fabrication of Multilayered Composite Nanofibers Using Continuous Chaotic Printing and Electrospinning: Chaotic Electrospinning. *ACS Appl. Mater. Interfaces* **13**, 37455–37465 (2021).

ABSTRACT OF THE DISSERTATION

Nanoscale IR Spectroscopy Based on Molecular Optomechanical Damping

by

Mohammad A. Almajhadi

Doctor of Philosophy in Electrical Engineering and Computer Science

University of California, Irvine, 2021

Professor H. Kumar Wickramasinghe, Chair

The quest to beat the diffraction limit and map sample optical properties with nanoscale spatial resolution led to new techniques of performing microscopy and spectroscopy. Among these techniques is scanning probe microscopy (SPM). SPM relies on a mechanical sensor (a cantilever) with a tip terminated by a nanometer radius apex that is interacting with a sample surface via van der Waal's forces which extends a few nanometers from sample surface; the radius of the apex determines the interaction volume which in turn determines the spatial resolution. Coupling the electromagnetic field to the apex focuses it to a volume with nanoscale dimensions limited by the apex radius, which can be exploited to prob sample chemical information with nanoscale spatial resolution. With the advent of the advanced nanoscale fabrication processes, tips with apexes of a few nanometers radius become commercially available making SPM an ideal alternative for the conventional, diffraction-limited optical microscopy and spectroscopy. Aperture and apertureless scanning near field optical microscopy are the 1st demonstrations that combine the SPM with optical light source, where sample optical properties down to a few tens of nm have been resolved. To perform nanoscale

spectroscopy using SPM, the cantilever either acts as a nano-scattering object to convert the evanescent near-field into propagating far-field or as a force sensor to directly measure near-field optical force. The near-field optical force can be probed while the cantilever tip is in contact with the sample or in non-contact. Over the last decade, the trend of using a cantilever as a force sensor for spectroscopic application continues to rise largely due to the simplicity of the experimental setup, high SNR, and high special resolution.

Infrared photoinduced force microscopy (IR-PiFM) is becoming the standard technique to probe the near-field optical force in non-contact mode. Here, sample chemical properties can be resolved with special resolution better than 10 nm and with monolayer sensitivity. Since PiFM invention (2010), the contrast mechanism is still under debate. This is largely due to the simultaneous electromagnetic excitations of the photothermal-induced and dipole-induced forces, and their interplay with van der Waal's forces. All the proposed mechanisms for IR-PiFM assume near-field tip-sample optical interaction is conservative. However, this assumption has not been validated experimentally. In this dissertation, we experimentally investigate the contrast mechanism of IR-PiFM for recording vibrational resonances. We demonstrate that the optically vibrating molecules damp the oscillating cantilever, where the damping force is dependent on sample complex refractive index. Thus, the measured spectroscopic information of a sample is directly related to the wavelength dependent energy lost in the oscillating cantilever.

1 Amplitude modulation atomic force microscopy

1.1 Introduction

Atomic force microscopy (AFM) is a nanoscale imaging technique that relies on a mechanical transducer (prob) which translates a specific nanoscale interaction energy into mechanical energy. This mechanical prob can be a rectangular cantilever terminated with a sharp tip (with nanometers radius). The prob is brought into sample surface with high precision using control loop configuration depending on the state of the prob. Generally, the probe can be in oscillating state or static state. These states are called AFM modalities. When the probe is brought nanometers from sample surface, the tip-sample interactions are transduced into mechanical deflection. This deflection can be read as a DC bending governed by simple Hook's Law or a change in the oscillating amplitude reflecting the strength of the interaction energy. AFM modalities can be classified, broadly, into contact mode AFM (cAFM) and dynamic mode AFM (dAFM). In fact, the 1st AFM ever was operated using contact mode, largely due to its simplicity¹. One year later, dAFM was invented². In contrast to the contact mode which load a sample surface with μN to nN forces laterally and vertically which might cause irreversible damage, in dynamic mode the cantilever tip oscillates near sample surface with small to no vertical forces and effectively no lateral forces. Thus, it is not surprising if dAFM becomes the choice for soft samples such as biological and polymer samples. The image of a sample is constructed by raster scan the sample, where the interaction energy is recorded for each pixel. In this brief introduction, we will discuss the tip-

sample interactions in dAFM mode as it is relevant to the thesis and leave contact mode for the reader to investigate.

In 1987, H. K. W.'s group announce the birth of dAFM². They were able to map sample topography by keeping the tip-sample force gradient constant while scanning the sample. Basically, the cantilever was vibrated using a piezoelectric transducer at resonance and the oscillation amplitude were measured using laser heterodyne interferometer. This oscillation amplitude was used as a feedback signal to fix tip-sample averaged distance, hence fixed force gradient. Because the oscillation amplitude of the probe is monitored, the technique was coined amplitude modulation AFM (AM-AFM). Most of today AFM operate with similar experimental apparatus except for laser heterodyne interferometer, where it has been replaced by position sensitive detector method³. Several emerging techniques relying on AM-AFM have been invented; Kelvin probe force microscopy⁴ (maps sample electrical properties), and scattering scanning near-field optical microscopy^{5,6} are but a few examples.

Normally the oscillation amplitude is controlled using lock-in amplifier (LIA). This LIA outputs the phase and the RMS amplitude of the oscillating cantilever. It turned out that the amplitude channel cannot be used to map sample mechanical/chemical properties. The phase channel, on the other hand, was found to be dependent on mechanical/chemical properties^{7,8}. In 1998, Cleveland et. al. showed experimentally that the phase of the oscillating cantilever in AM-AFM is sensitive to dissipative tip-sample interaction while the oscillating amplitude is sensitive to conservative and dissipative

interactions⁹. As will be explained, conservative interactions change the compliance of a cantilever, while dissipative interactions change its quality factor. Currently, all AM-AFM simultaneously extract the topography, induced by keeping the oscillating amplitude fixed, and local dissipative interactions by recording the change in the phase channel.

In this chapter, AM-AFM experimental apparatus will be introduced. The van der Waals interactions between a sphere and plane surface will be explained to understand how tip-sample interaction takes place. Then, the conservative and dissipative tip-sample interactions will be explained. For example, the effect of the conservative interactions on the cantilever and the sources of dissipation will be discussed. Finally, available experimental methods that can decouple conservative and dissipative interactions for quantitative measurement will be introduced briefly.

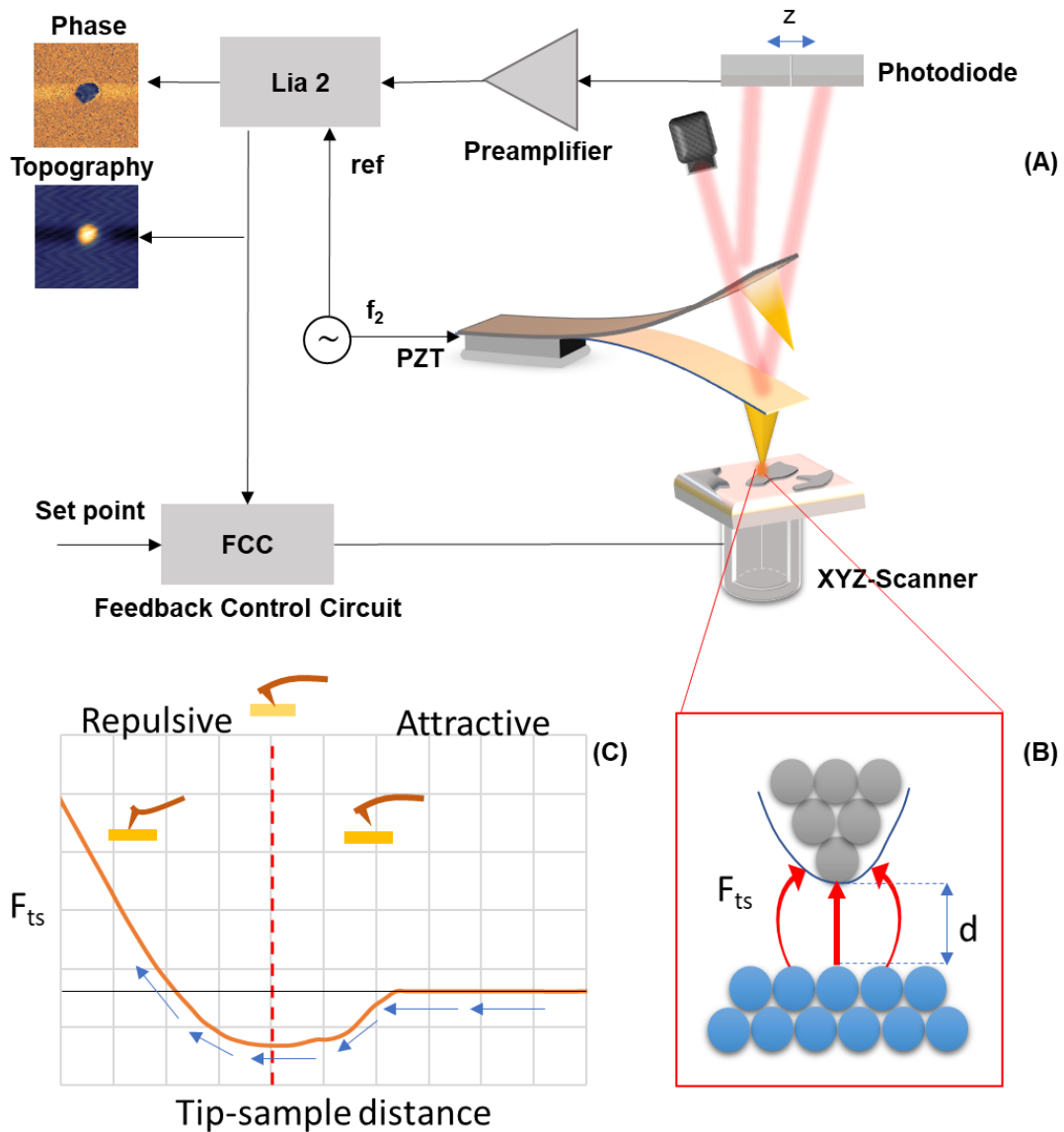


Fig. 1 Atomic force microscopy apparatus (A). Close look to the tip-sample junction (B). Force-distance curve extracted using contact mode AFM (C).

1.2 Tip-sample van der Waals interactions (sphere-plane model)

When tip is brought to the sample surface, attractive van der Waal's (vdW) forces act on the tip causing the cantilever to bend into the sample surface till the tip snap to contact

with the sample. Fig. 1(C) shows an example of vdW interaction forces measured by recording cantilever deflection while approaching the cantilever towards sample surface using contact mode AFM. Note that these forces are mostly negative (attractive) except for the very small range where tip deflection is reverse. The minimum point in the curve determines the contact point with the sample surface. At this contact point repulsive vdW interactions take over. The equation that describes the observed curve in Fig. 1(C) can be written¹⁰

$$F_{\text{DMT}}(d) = \begin{cases} -\frac{HR_t}{6d^2} & , \quad d > a_0 \\ -\frac{HR_t}{6a_0^2} + \frac{4}{3}E_{\text{eff}}\sqrt{R_t}(a_0 - \delta)^{1.5}, & \delta < a_0 \end{cases} \quad (1)$$

Where a_0 is the spacing between atoms which, in solids, is about 0.2-0.3 nm. H , R_t , and d are Hamaker's constant, tip radius, and tip-sample averaged distance respectively. The effective Young's modulus and deformation (in nm) are E_{eff} and δ respectively. Equation 1 is derived using Derjaguin-Muller-Toporov (DMT) contact model¹¹. The main driving forces in vdW forces are the dispersion forces. Dispersion forces (or London forces) are the results of a fluctuating atoms that generate instantaneous dipole moment which is imaged by adjacent atoms. Since all material are polarizable, London forces always exist between tip and sample. Other form of forces that contribute to the overall vdW interaction are Keesom and Debye forces, but those forces require molecules with permanent dipole moments, a condition that is not always met.

When tip senses the vdW forces, it will bend such that the vdW forces are balanced by the spring force. Once the gradient of vdW forces is larger than the spring const of the

cantilever, the tip will jump to contact. This jump-to-contact distance D depends on the following parameters

$$D = \sqrt[3]{\frac{HR_t}{3k_{\text{eff}}}} \quad (2)$$

Where k_{eff} is the effective spring constant of the tip-sample system. The total force required to separate the tip and sample is called the pull off force. Note that D can be minimize by increasing tip stiffness and decreasing tip radius.

When tip jump to contact, one can extract mechanical properties of a sample. The contact mechanics of tip-sample system can be modeled using Hertz, DMT or Johnson, Kendall and Roberts (JKR) models^{11,12}. Let's start with the simplest, the Hertz model. Let's assume that the tip and sample can be modeled as two interacting spheres with radius R_1 and R_2 . Hertz said when those spheres are brought to contact and if we apply force (F_{ap}) to press them, the two spheres will deform. Thus, a contact area A with radius r will be formed due to the deformation. As F_{ap} increases r increases, hence A increases. Hertz equations for contact radius r , the deformation δ , effective radius R_{eff} , and effective Young's modulus E_{eff} are

$$r = \left(\frac{3F_{\text{ap}}R_{\text{eff}}}{4E_{\text{eff}}} \right)^{\frac{1}{3}} \quad (3)$$

$$\delta = \frac{r^2}{R_{\text{eff}}} = \left(\frac{9F_{\text{ap}}^2}{16E_{\text{eff}}^2R_{\text{eff}}} \right)^{\frac{1}{3}} \quad (4)$$

$$R_{\text{eff}} = \left(\frac{1}{R_1} + \frac{1}{R_2} \right)^{-1} \quad (5)$$

$$E_{\text{eff}} = \left(\frac{1 - \nu_1^2}{E_1} + \frac{1 - \nu_2^2}{E_2} \right)^{-1} \quad (6)$$

ν_1 and ν_2 are the poisson ratio of sphere 1 and 2 respectively. From the deformation δ , normal stiffness or contact stiffness (k_{ts}) can be written as

$$k_{\text{ts}} = \frac{\partial F_{\text{ap}}}{\partial \delta} = 2E_{\text{eff}}\sqrt{R_{\text{eff}}\delta} = 2rE_{\text{eff}} \quad (7)$$

Note that the normal stiffness or contact stiffness value depends on the applied load. Unlike usual spring constant we know from Hook's law, where the stiffness of a spring remains constant regardless to the applied force, k_{ts} increases as the applied force increases. For Hertz model to work, the following assumptions must be met¹³:

- 1- The interacting spheres are perfectly smooth and homogeneous with no surface coatings or films.
- 2- The elasticity of the interacting spheres is linear.
- 3- No in-plan forces that induce friction between the two spheres.
- 4- The contact radius r and the deformation δ are much smaller than the radius of the interacting spheres.

Note that in Hertz model the adhesive forces are neglected and the deformation is induced only by the applied forces F_{ap} . DMT model is essentially similar to Hertz model but the adhesion force F_{adh} (mainly vdW forces) is included in the total applied force. However, F_{adh} is assumed to be weak so that the contact area and deformation deviate a little from the values estimated by Hertz equations. In JKR model, it assumes that the F_{adh} is strong enough to cause significant increase in the contact area and deformation. Thus, increasing the contact radius r . In general, DMT model is used when stiff sample that exhibit weak, long range adhesive force are imaged. On the other hand, soft

sample with strong, short range adhesive forces is modeled with JKR. Apparently JKR and DMT are the extreme limits for soft and stiff samples. In DMT model, Eq. (3) and Eq. (4) remain the same but with F_{ap} replaced by $F_{ap} + F_{adh}^{DMT}$, $F_{adh}^{DMT} = 2\pi R_t W$. W is the energy needed to separate the tip and sample from each other. Because in JKR model $F_{adh}^{JKR} = \frac{3}{2} \pi R_t W$ is assumed to cause significant deviation from values predicted by Hertz model, Eq. (3) and Eq. (4) are written as

$$r = \left(\frac{3R_{eff}}{4E_{eff}} \left[F_{ap} + 3W\pi R_{eff} + \sqrt{3W\pi R_{eff} F_{ap} + (3W\pi R_{eff})^2} \right] \right)^{\frac{1}{3}} \quad (8)$$

$$\delta = \frac{r^2}{R_{eff}} - \left(\frac{2\pi W r}{E_{eff}} \right)^{\frac{1}{3}} \quad (9)$$

Note that Eq. (9) implies that in soft material the deformation is lowered, and the contact radius increases. However, if the material is very stiff, then Eq. (9) is approximated by the Hertz equation (Eq. (4)).

Thus far the cantilever was assumed to be in static mode. In the following section, the tip-sample interaction will be analyzed while the cantilever is in dynamic mode.

1.3 Tip-sample conservative and dissipative interactions

To understand how an oscillating tip interacts with the sample, driven damped harmonic oscillator will be used to model the oscillating cantilever, and the time-independent tip-sample interaction force (F_{ts}) will be included. Lets assume the cantilever base is excited sinusoidally with A_d and ω_d as $z_d = A_d \cos(\omega_d t)$. As a result, the cantilever will

start oscillating at the same frequency but with phase lag and different oscillation amplitude as $z_c = A_0 \cos(\omega_0 t + \varphi)$. The equation of motion can be written as

$$\frac{d^2 z}{dt^2} + \sqrt{\frac{k}{m}} \frac{1}{Q} \frac{dz}{dt} + \frac{k}{m} (z - z_d) = F_d + F_{ts} \quad (10)$$

Here F_d is the driving force and k is the cantilever stiffness measured far from sample surface. Since F_{ts} is highly nonlinear function, Eq. (10) is normally solved numerically. However, if small oscillation amplitude is assumed such that F_{ts} is nearly linear across the oscillation amplitude (small oscillation amplitude limit), Eq. (10) can be solved analytically. What we want to know from Eq. (10) is simply the steady state oscillation amplitude and phase of the cantilever under the influence of F_d and F_{ts} . Without going into the mathematical derivation, the solution will be $z_c = A_0 \cos(\omega t + \varphi)$, where the free amplitude A_0 (measured far from sample surface) and phase of the cantilever will be

$$A_0 = \frac{A_d}{\sqrt{(1 - r_a^2)^2 + \frac{r_a^2}{Q_{\text{eff}}^2}}} \quad (11)$$

$$\varphi = \arctan\left(-\frac{r_a}{Q_{\text{eff}}[1 - r_a^2]}\right) \quad (12)$$

r_a is the ratio between $\omega_d/\omega_{\text{eff}}$ and $\omega_{\text{eff}} = \omega_0 + \delta\omega$, where $\delta\omega = \frac{\omega_0}{2k} \frac{dF_{ts}}{dz} = \frac{\omega_0}{2k} k'$ is the shift in the cantilever frequency induced by tip-sample force gradient; the force gradient is solved around the equilibrium position. The resonance frequency of a damped harmonic oscillator (ω_0) with a mass m can be written as

$$\omega_0 = \sqrt{\frac{k + k'}{m}}, \quad \text{where } k' = \frac{dF_{ts}}{dz} \quad (13)$$

Note that the change in frequency is governed by the tip-sample force gradient. This type of interaction is conservative because it does not imply any energy dissipation in the system; only the cantilever compliance is changing. Note also, the force gradient modifies the cantilever stiffness by $k' = dF_{ts}/dz$. Thus, the $k_{eff} = k + k'$. Now depending on the sign of the force gradient, k_{eff} either increases (positive $\delta\omega$) or decreases (negative $\delta\omega$). The effective quality factor Q_{eff} includes any dissipative processes during tip-sample interaction and air damping. Equation (11) and (12) shows that both conservative and dissipative interactions induce change in A_0 and φ .

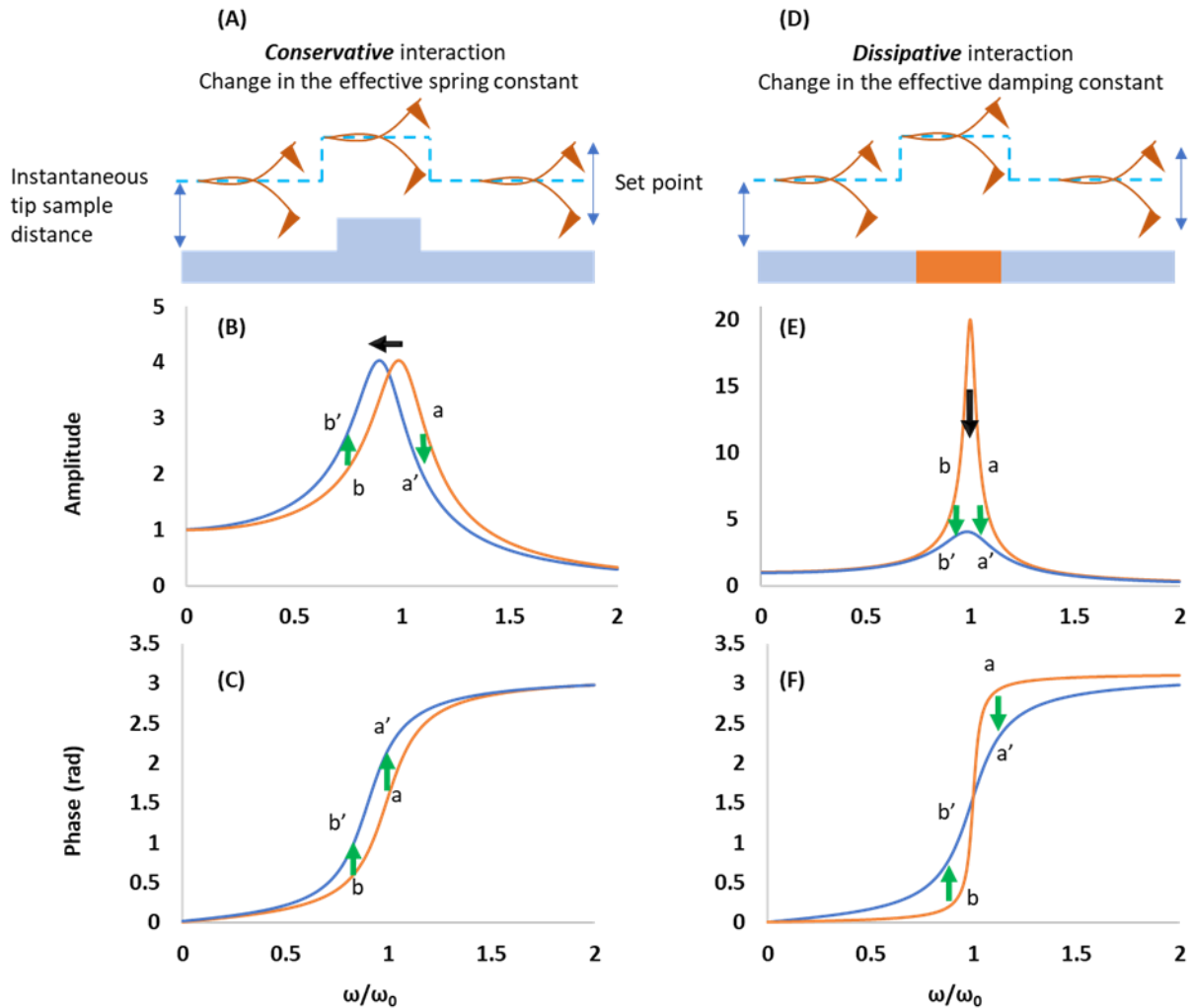


Fig. 2 Conservative and dissipative tip-sample interactions (A) and (D). The change in the oscillation amplitude due to conservative (B) and dissipative (E) interactions. The change in the oscillation phase due to conservative (C) and dissipative (F) interactions.

The cantilever, in AM-AFM, is excited near resonance, where the slope of the amplitude curve is maximum. Once the cantilever is engaged with the sample, conservative interactions and dissipative interactions reduce the oscillating amplitude through frequency shift and reduction in the quality factor respectively. For conservative

interactions, the van der Waal's forces (F_{ts}) load the cantilever with attractive or repulsive forces. When the forces are attractive, k^* is negative. Thus, the cantilever compliance is lowered. This leads to pushing the cantilever resonance to lower values. Repulsive forces, on the other hand, push the cantilever resonance to higher values because k^* is positive. This frequency shift, during imaging, cannot be detected directly using AM-AFM because in this modality the change in amplitude is detected not frequency shift, and the cantilever is driven at a fixed frequency during imaging.

Dissipative interactions, on the other hand, reduce the oscillating amplitude by reducing the quality factor of the cantilever. The reduction in Q is induced by several dissipative mechanism. Surface energy and adhesion hysteresis are two major dissipation channels. Hysteresis implies that the strength of tip-sample interactions during the 1st half cycle (approaching half cycle) is different from the 2nd half cycle (retracting half cycle). Meaning, the work done by the cantilever becomes path dependent. Thus, energy will be dissipated. The other dissipative channel is viscoelasticity. This effect is related to the molecular displacement with the tip motion and/or thermal excitation due to atomic collisions and/or breaking/disturbing chemical bond. This effect is strong in soft samples such as polymers¹⁴.

To quantify the energy dissipated by the tip-sample interaction power balance equation will be used¹⁵. In this equation, the delivered averaged power to the cantilever must equal the power dissipated by the cantilever. The cantilever dissipate energy due to air damping and tip-sample interaction. The former can be considered as a background

dissipation (independent of tip-sample interaction). For simplicity, the squeeze film effect will not be considered. The averaged mechanical power delivered to the cantilever $\langle P_{in}^m \rangle$ and the averaged dissipated power $\langle P_{diss}^c \rangle$ primarily caused by air damping can be written as

$$\langle P_{in}^m \rangle = \frac{1}{2} A_{ts} A_d k \omega_d \sin(\varphi) \quad (14)$$

$$\langle P_{diss}^c \rangle = \frac{1}{2Q} k A_0^2 \omega_d \quad (15)$$

A_{ts} is the cantilever oscillation amplitude once tip-sample interaction is included (tip is engaged with the sample). Thus, A_{ts} is always smaller than the free oscillation amplitude $A_0 = Q A_d = A_{ts} + \delta A$ measured far from sample surface. δA is the amount of amplitude change induced by tip-sample interaction. A_{ts} is kept fixed during scanning, and the ratio A_{ts}/A_0 is the setpoint determined before tip engages with the sample. If $\langle P_{diss}^{ts} \rangle$ is the averaged power loss due to tip-sample dissipative interactions, from power balance, we can write

$$\langle P_{diss}^{ts} \rangle = \langle P_{in}^m \rangle - \langle P_{diss}^c \rangle \quad (16)$$

Combining Eq. (14), (15) and (16) gives

$$\langle P_{diss}^{ts} \rangle = \frac{k A_{ts}^2 \omega_0}{2Q} \left(\frac{A_0 \sin(\varphi)}{A_{ts}} - 1 \right) \quad (17)$$

Here we assumed that $\omega_d = \omega_0$. Solving for A_{ts} gives

$$A_{ts} = A_0 \sin(\varphi) \left(\frac{\langle P_{diss}^{ts} \rangle}{\langle P_{diss}^c \rangle} + 1 \right)^{-1} \quad (18)$$

From Newtons equation of motion for a damped oscillating cantilever, we can relate rate of dissipated mechanical power $\langle P_{diss}^c \rangle$ due to air damping to damping constant Γ_c

through $\langle P_{\text{diss}}^c \rangle = 0.5m\Gamma_c\omega_d^2A_0^2$ (where m is the effective mass of the cantilever), we can therefore write Eq. (18) in terms of Γ_c and Γ_{ts} .

$$A_{\text{ts}} = QA_d \sin(\varphi) \left(\frac{\Gamma_{\text{ts}}}{\Gamma_c} + 1 \right)^{-1} \quad (19)$$

Note that Eq. (19) implies that if tip-sample interaction is assumed to be purely conservative then the phase will depend on the setpoint A_{ts}/A_0 , and since the setpoint is always fixed, Φ never changes.

In contrast to the static AFM in which cantilever deflection and stiffness are the only experimental parameters that need to be considered prior imaging, there are many parameters that needs to be either set or measured in AM-AFM:

- The deriving amplitude A_d (set) and the oscillation amplitude A (measured).
- The phase between deriving signal and cantilever oscillation Φ (measured).
- Deriving frequency ω_d (set), the cantilever resonance ω_o (measured), and the frequency shift $\delta\omega$ (measured).
- The cantilever stiffness k (measured) and the quality factor Q (measured).

2 Photoinduced force microscopy

2.1 Introduction:

Soon after the invention of scanning tunneling microscopy (STM)¹⁶, scientists realized that with such technique, one can probe sample properties of interest with interaction volume and spatial resolution limited by tip radius. Among the 1st field to take advantage of STM apparatus is optical microscopy. For example, D. W. Pohl et al successfully demonstrated the 1st optical microscope that uses chemically sharpened optical fiber coated with thin film of aluminum except for the apex which was used as nano aperture¹⁷. The light was guided through the optical fiber and the sample was illuminated through the nanoaperture. The authors were able to beat the diffraction limit and achieved a spatial resolution of $\lambda/20$, where λ is the light wavelength. This technique further investigated, and in 1988 was coined as near-field scanning optical microscopy (NSOM) and reviewed by the same group^{18,19}. In 1990, H. K. Wickramasinghe and C. C. William invented apertureless NSOM (aNSOM)²⁰. This method utilized dAFM apparatus to control tip-sample spacing, and the vibrating tip apex acts as a nano scatterer or a nano antenna. The scattered light is then collected in the far field. With aNSOM, the limitations of NSOM regarding the maximum input power and aperture size has been surpassed. Today, aNSOM dominates the field of nano optical microscopy, and it becomes a solid technique with solid theoretical and experimental understanding. aNSOM is reviewed here²¹. NSOM and aNSOM belong to the optical probe microscopes that measure optical sample properties by measuring the change in the detected amplitude and phase of the electromagnetic field induced by a change in

sample optical properties. This optical detection setup is at the far field which consists of photodiode and optical tools such as objectives, lenses, and beam splitters.

Other set of optical microscopes probe sample optical properties directly through registering cantilever deflection. Here, the optically induced forces and gradient forces cause the cantilever to deflect if it is in static state or the oscillating amplitude to change if the cantilever is in dynamic state. Because the cantilever acts as optomechanical sensor, far-field optical detection setup is not necessary. In the case of dAFM, the near-field optical forces and its gradient cause a change in the cantilever oscillation amplitude conservatively and/or dissipatively similar to the van der Waals tip-sample interaction which can be conservative in some cases and dissipative in another.

Conservative tip-sample optical interactions can be attractive or repulsive, and this type of interaction cause a change in the cantilever compliance; it either shifts the location of the cantilever resonance to lower values (attractive) or to higher values (repulsive). The dissipative interactions reduce the quality factor of the cantilever resonance leading to a reduction in the oscillating amplitude.

The simplicity of directly detecting the optical forces by the AFM cantilever comes at the cost of the difficulty of interpreting the measured signal. In the near-field, several competing forces contribute to the registered signal. These forces can be broadly categorized into forces of electromagnetic origin and forces of photothermal origin.

Although they act in a different time scale, decoupling these forces may not be a straightforward task when measured in non-contact or tapping AFM modes. In additions, the local optical forces can be conservative and/or dissipative depending on

the experimental conditions. Thus, adding an additional order of magnitude in the complexity to interpret the registered signal.

The electromagnetic forces are modeled by replacing the sample and tip with two spheroid objects with polarizabilities α_s and α_t respectively. When sample is illuminated, the local electric field polarizes the sample resulting in a dipole moment $P_s = \alpha_s E_{loc}$. P_s is imaged by the tip, which can be static or vibrating, resulting in a dipole moment at the tip $P_t = \alpha_t E_{loc}$; note that the presence of the tip enhances the local field E_{loc} . These two interacting dipoles apply an attractive force that pulls the cantilever towards the sample resulting in a change in the oscillating amplitude or in the dc deflection. The photothermal forces originate from the locally absorbed electromagnetic energy by the tip and sample. The subsequent effect of the optical absorption is an increase in sample temperature causing thermal stresses which are relaxed by thermal expansion. If the tip is in contact with the sample, the local thermal expansion causes a repulsive force, but if the tip is in non-contact with the sample, the thermal expansion changes the strength of the vdW force leading to an attractive force. Because the materials polarizability is wavelength dependent, one can extract the chemical information about a sample by registering the wavelength-dependent forces with nanoscale spatial resolution.

Recently, several spectroscopic techniques have been developed to probe near-field optical interactions. For example, photothermal induced resonance (PTIR) and peak-force infrared (PFIR) register the mechanical action of local thermal expansion induced by local optical absorption when tip is in contact with sample^{22,23}. The spatial resolution

of these techniques is in the order of 10 nm. However, in this dissertation we will focus and discuss another high-resolution, non-contact spectroscopic technique named as photoinduced force microscopy introduced by H. K. Wickramasinghe et al in 2010²⁴. Photoinduced force microscopy (PiFM), operating in non-contact AM-AFM mode, probes near-field optical forces by registering the change in the cantilever oscillation amplitude. A laser source is focused on the tip-sample junction and the excited molecules interact with the tip, and the strength of the interaction is wavelength dependent. In other words, when the molecules/atoms excited on resonance (vibrational or electronic transition resonance), the interaction becomes detectable. This interaction can be further enhanced by modulating the near-field interactions at f_m such that the photoinduced forces are sensed at one of the cantilever bending modes. In this case, the photoinduced forces are enhanced by the quality factor of the cantilever resonance. Two main modalities for operating PiFM. The 1st is the heterodyne mode, and the 2nd is homodyne mode. In heterodyne mode, the cantilever oscillating at f_c senses the nonlinear vdW interaction in the vicinity of the sample surface; this nonlinearity allows for mixing two different tip-sample interactions. This mixing causes the cantilever to oscillate at the sideband frequencies located at the sum and the difference of f_m and f_c ($f_c \pm f_m$). If one of the sidebands is tuned to coincide with one of the mechanical resonances of the cantilever, the oscillation is enhanced by the quality factor, hence the near-field optical forces are enhanced. Because nonlinear vdW forces are effective only near tip apex, only optical forces act on the tip apex are mixed. Thus, heterodyne PiFM is sensitive to local near-field optical forces, where the volume of local interaction is limited by the tip radius. In homodyne PiFM, the near-field optical forces are modulated

directly at one of the cantilever resonances. Here the cantilever is excited photothermally on top of the tip-sample near-field optical interactions. This implies that homodyne PiFM suffers from background signal that might overcome the local optical interaction.

2.2 The debate

Till now we have not discussed the contrast mechanism of PiFM. In other words, what is the nature of the near-field optical forces responsible for the observed PiFM signal? In this section, we will summarize the different opinions/theories that tried to address the contrast mechanism of homodyne and heterodyne PiFM.

When PiFM was introduced in 2010, the photoinduced force was explained to be mediated by the photoinduced dipole moment of a polarizable sample. This dipole moment is mirror imaged by the tip which is coated by thin film of platinum to enhance the near-field interaction. The dipole and its mirror image interact generating gradient force (F_g) proportional to the tip and sample polarizabilities. Because tip polarizability is known in advanced, sample polarizability can be extracted by measuring F_g . Here, F_g is assumed to be the responsible for the observed PiFM signal. In addition, F_g depends on the real part of the product of the tip and sample polarizabilities $F_g \propto \text{Re}\{\alpha_s^* \cdot \alpha_t\}$, and derived by analyzing the optical tip-sample interactions using the dipole-dipole coupling theory²⁴. Here, the sample resonances are of the electronic transition types, where the excitation wavelength is in the visible region.

When PiFM was extended to probe vibrational molecular resonance in the infrared region²⁵, the prediction of the dipole-dipole coupling theory (DD) and the experimental observations conflicted with each other. While the DD predict F_g to show dispersive spectral signature of the vibrational molecular resonance (following the real part of the complex refractive index), the experimental results showed dissipative spectral signature (following the imaginary part of the complex refractive index). Consequently, alternative contrast mechanisms have been proposed by several scientific groups. All of them assumes that the PiFM signal, in IR region, stems from photothermal expansion.

In one study, the PiFM is thought to be sensitive to the short-range thermal expansion, which are measured when tip is in contact with the sample²⁶. Here operating PiFM in tapping mode is implied. In their study, the F_g was calculated numerically and found to be in fN range, where the tip and sample were modeled as two spheres with radius r . The same group suggested, in a different study, that when heterodyne PiFM is operating in non-contact regime, photoacoustic forces dominate the signal²⁷. Note that photoacoustic and short-range forces are repulsive and assumed to be conservative. However, F_g was theoretically analyzed with Green's function and found to be in pN range²⁸. Furthermore, a more realistic numerical calculation showed that F_g is indeed in the pN range, where the tip was modeled as conical shape terminated by a sphere with radius r , and the substrate effect has been taking into account²⁹. In addition, several groups showed that the photoinduced force is attractive not repulsive^{30,31}. Thus, short range repulsive thermal expansion and long repulsive photoacoustic force have been dismissed as possible contrast mechanisms for heterodyne PiFM. However, showing F_g

to be in pN range, added further confusion: if the F_g is in pN range for infrared vibrational resonance, then why the spectral line shape when measured by PiFM is dissipative? Clearly another force stronger than F_g dominates the measured signal and depend on the imaginary refractive index. To unravel the nature of this force, one group proposed vdW-mediated thermal (F_{vdW}^{th}) expansion as the origin of PiFM signal; the strength of the vdW attractive forces that act on the cantilever near sample surface changes upon photothermal expansion due to a change in the tip-sample spacing³². Here operating PiFM in noncontact mode is implied. Note that F_{vdW}^{th} is attractive and conservative, and it follows dissipative spectral line shape. If F_{vdW}^{th} is the contrast mechanism, then in homodyne PiFM, F_{vdW}^{th} is measured, while in heterodyne PiFM, ∇F_{vdW}^{th} is measured. However, this hypothesis suggested that a monolayer with thermal expansion of a few pm may not be detectable. Note that all the aforementioned studies assumed that the photoinduced force is conservative. However, no experimental evidence was shown to prove their assumption.

In this dissertation, the contrast mechanism of heterodyne PiFM will be investigated, and the aforementioned hypothesis will be challenged. First, a details numerical analysis to quantify the gradient forces will be introduced. In this section, the gradient forces for a vibrational resonance and plasmonic resonance are shown to be ranging from 10s to a few 10s of pN. For plasmonic resonance, F_g is mostly dissipative, while dispersive for molecular vibrational resonance. Then, a series of experiments aiming at unravelling the contrast mechanism of heterodyne PiFM will be introduced. In this

section, we will experimentally test those hypotheses one by one through extensive experimental observations. Then, the alternative contrast mechanism will be proposed.

2.3 Contrast and imaging performance in photo induced force microscopy

2.3.1 Introduction

Lateral and vertical imaging performance in the visible and infrared are analyzed numerically. In addition, spherical particle with 5 nm radius is impeded in a dielectric thin film to test the subsurface imaging performance of the PiFM. In this section, two major questions will be answered. The 1st is related to the dependence of the local gradient force (F_g) on the excitation wavelength (λ) when the object is excited across one of its optical resonance using a tunable laser source. The 2nd is related to whether F_g force is detectable when measured by atomic force microscopy (AFM). AFM sensitivity is in pN range; therefore, the local photoinduced forces must be in the pN range otherwise it will not be detected. As will be explained later, this is not the full story. In fact, as it is clear to the expert in PiFM, the mechanical action of the local electromagnetic wave induced by local absorption consists of many competing forces. However, in this section we will assess F_g that is directly proportional to the dipole moment and the gradient of the local field. The strength of F_g is assessed for metal (gold), polymers (Polystyrene and Polymethylmethacrylate), and solid (SiC).

We, first, introduce a brief theory of the gradient force followed by introducing our basic simulation set up and parameters used in the numerical simulation. Then, we validate our simulations against closed form solutions for optical forces on an isolated nano sphere obtained from Mie theory. After that, we calculate the forces between tip and

sample using maxwell stress tensor formalism under different conditions. The results will be discussed followed by brief concluding remarks.

2.3.2 Brief theory of near field optical forces in PiFM

PiFM senses near field optical force directly by registering the optomechanical action on the cantilever. The stronger the tip-sample optical force the larger the deflection signal of the AFM cantilever. Thus, we are interested in calculating the optical force on the tip. The detected force in PiFM is related to the tip and sample polarizabilities; if the tip polarizability response is known, chemical information can be extracted about the sample with spatial resolution limited by the tip radius. In earlier work, a dipole-dipole coupling approximation was used to analyze the photoinduced force between tip and sample upon optical excitation^{33,34,35}. The tip and sample, in this approximation, are assumed to be dipolar spheroids with dipole moments \mathbf{P}_t and \mathbf{P}_s respectively. This approximation is useful for qualitative analysis, i. e., it can be useful for studying the underlying physics and trends of the photoinduced force. In the electrostatic approximation, the time averaged optical gradient force calculated at the tip or sample particle $\langle \mathbf{F}_{\text{opt}}^{t,s} \rangle$ can be written as

$$\langle \mathbf{F}_{\text{opt}}^{t,s} \rangle = \frac{1}{2} \text{Re}\{(\mathbf{p}_{t,s}^* \cdot \nabla) \mathbf{E}_{\text{loc}}^{t,s}\} \quad (20)$$

where,

$$\mathbf{E}_{\text{loc}}^{t,s} = \mathbf{E}_{\text{inc}} + \frac{\mathbf{P}_{s,t}}{2\pi\epsilon_m\epsilon_0 r^3} \quad (21)$$

and \mathbf{E}_{loc} and \mathbf{E}_{inc} are the local electric field and excitation field, respectively. All quantities typed in bold are in phasor form. The subscript t and s refer to tip and sample

respectively. ϵ_m and ϵ_0 are the dielectric constant of the media and the permittivity of free space respectively. The asterisk indicates the complex conjugate. Since we measure the gradient force in PiFM, the scattering force has been omitted in Eq.(20). If we consider the tip dipole to be at the origin of our coordinate system, then the sample dipole is located at a radial distance r from this origin. The optically induced dipole moment of the tip or the sample is proportional to the local electric field at \mathbf{P}_t or \mathbf{P}_s

$$\mathbf{P}_{t,s} = \alpha_{t,s} \mathbf{E}_{loc}^{t,s} \quad (22)$$

where $\alpha_{t,s}$ is the tip/sample complex polarizabilities, and it is defined as $\alpha_{t,s} = \alpha'_{t,s} + i\alpha''_{t,s}$, where $\alpha'_{t,s}$ and $\alpha''_{t,s}$ are the real and imaginary component of $\alpha_{t,s}$. By substituting Eq. (21) and (22) into Eq. (20), we see that the time averaged optical force will be proportional to the product of the real part of α_t and α_s as

$$\langle F_{opt,z} \rangle = -\frac{3\alpha'_t \alpha'_s}{2\pi Z^4} E_{0z}^2 \quad (23)$$

The term $\alpha''_t \alpha''_s$ is omitted from Eq. (23) because it is 2-3 orders of magnitude smaller than $\alpha'_t \alpha'_s$. Therefore, chemical information can be extracted by studying the force spectrum behavior over the optical absorption band of the sample.

Here, we will be using detailed 3D electromagnetic simulations to understand the contrast and imaging performance in PiFM. Maxwell stress tensor ($\vec{\mathbf{T}}$) formulation will be employed to calculate $\langle \mathbf{F}_{opt} \rangle$ on the tip under different conditions, where $\langle \mathbf{F}_{opt} \rangle$ can be written as

$$\langle \mathbf{F}_{opt} \rangle = \oint \langle \vec{\mathbf{T}}(\mathbf{r}, t) \rangle \cdot \tilde{\mathbf{n}}(\mathbf{r}) da \quad (24)$$

$\tilde{\mathbf{n}}(\mathbf{r})$ is the normal vector to the tip surface and the surface integral is the closed surface of a volume enclosing the portion of the tip that produces significant fields. The $\vec{\mathbf{T}}$ can be expressed as

$$\vec{\mathbf{T}} = \epsilon\epsilon_0 \mathbf{E}\mathbf{E} - \mu\mu_0 \mathbf{H}\mathbf{H} - \frac{1}{2}(\epsilon\epsilon_0 E^2 + \mu\mu_0 H^2)\vec{\mathbf{I}} \quad (25)$$

The notation $\mathbf{E}\mathbf{E}$, $\mathbf{H}\mathbf{H}$, E^2 , H^2 and $\vec{\mathbf{I}}$ are the outer product of the electric field, the outer product of the magnetic field, electric field strength, magnetic field strength, and the unit tensor respectively³⁶. We compare our numerical results with those obtained using the simple closed form dipole-dipole analysis described earlier.

2.3.3 Problem setup

The tip-sample force gradient was calculated using a Finite Element Method (COMSOL Multiphysics software) with frequency domain approach. The three-dimensional geometry was meshed using a non-uniform meshing based on free tetrahedral elements. To minimize the meshing points in our numerical simulation, we applied dense mesh elements only in the vicinity of tip-sample region. The following simulation parameters are fixed in this section. The tip is silicon (Si) with 10° half angle terminated by a sphere with radius of 10 nm. Tip-sample gap is 0.5 nm, and the substrate is Si and assumed to be infinite. The particle, shown in Fig. 3(b), has radius 5 nm. A z-polarized standing wave composed of two monochromatic plane waves traveling in +x and -x directions each with electric field amplitude (E_0) of 10^6 [V/m]. The surrounding medium is air.

First, the effect of tip-coating thickness (T_{th}) and sample-coating thickness (S_{th}) on the local electric field enhancement ($E_{enh}=|E_{loc}/E_{inc}|$) and the gradient force exerted on the tip. Then, lateral and vertical confinement of local electric field were calculated along a - a' and b - b' segment respectively. Second, the force spectrum, calculated as the tip, over an absorption band were investigated for vibrational resonance in the IR and plasmonic resonance in the visible regions. Finally, we investigated the vertical and lateral subsurface imaging performance by calculating the gradient force induced by a particle with 5 nm radius. (b). The particle material has been considered as Polystyrene (PS), gold (Au), and hexagonal silicon carbide (SiC). The dielectric functions have been taken from^{37,38,39,40,41}.

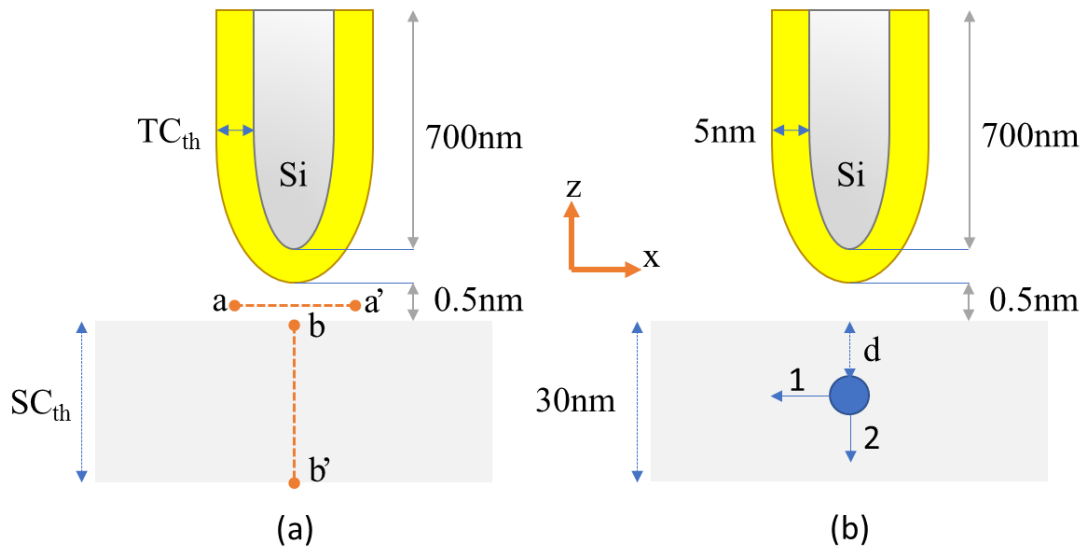


Fig. 3 The configuration set up. Tip, with 10° half taper angle, is terminated by spherical section of 100 Å radius. In (a), the tip is coated by metal with different coating thicknesses (T_{th}), and the Si substrate (not shown) is coated by a sample with different sample coating thicknesses (S_{th}). The amplitude of the electric field is calculated along a - a' and b - b' line segments. In (b), a particle 50 Å radius is placed at a depth d

within the sample. Arrows 1 and 2 indicate the sweeping direction of the particle. Tip-sample distance is 5 Å. The geometry is irradiated by standing wave with polarization parallel to the tip axis. Reference [29].

2.3.4 Bench marking against known closed form expression

Our numerical simulation was validated by implementing Mie scattering analysis simulations of optical forces and fields on particles and comparing the results to closed form analytical solutions.

Mie theory describes the scattering and absorption processes of an incident electromagnetic plane wave by a homogenous sphere. A sphere of 100 nm and refractive index $n = 5 + 0.4i$ surrounded by air has been modeled to extract the extinction and absorption cross sections. The extinction cross section (Q_{ext}) has been analyzed and compared to the analytical Mie solution done by Matzler code⁴². Our COMSOL simulation gave excellent agreement with Mie solutions (Fig. 4). Since Maxwell stress tensor (MST) formalism was employed for all force calculations, validating MST equations used by COMSOL was essential. Particles exposed to an incident field experience a radiation force along the incident direction. This force is proportional to the pressure cross section which in turn is proportional to the extinction and scattering cross sections. Once the pressure cross section is determined, the radiation force can be calculated. Radiation force must equal the integral of MST over the particle surface. Fig. 4 shows a comparison between the Mie solution and our

COMSOL results. The MST integral results are identical to the radiation force calculated by COMSOL and the Matzler code.

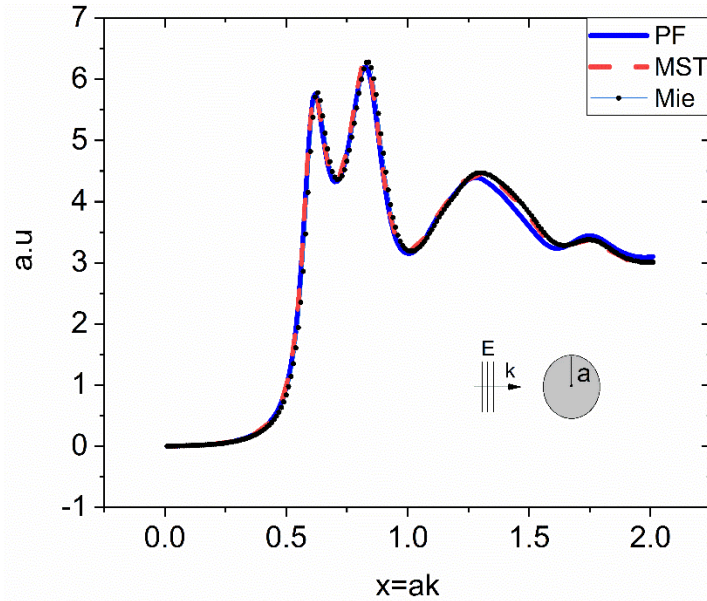


Fig. 4 MST and pressure force (PF) calculated by COMSOL, and PF calculated by Mie equations. Reference [29].

2.3.5 Effect of coating materials and thickness

In this section, we study the effect of T_{th} and S_{th} on E_{enh} in the tip-sample gap and on the gradient force exerted on the tip where the wavelength is 10 μm . The substrate is Si coated with PMMA. To assess the substrate effect on the field enhancement, the PMMA thickness was tuned till the E_{enh} started to saturate. Fig. 5(left column) shows two major results. The 1st, the thinner the sample thickness and coating thickness the higher the E_{enh} . Although E_{enh} saturates at S_{th} beyond 60 nm, E_{enh} is still present. Coating the tip with silver (Ag), platinum (Pt), or gold (Au) show no significant difference in the calculated E_{enh} .

The lateral resolution of PiFM, can be ascribed to the size of the volume of the electromagnetic fields at the tip apex. Here, we set sample thickness to 30 nm. and calculate the E_{enh} (see Fig. 3(a)) at different T_{th} . Fig. 6 shows the electric field calculated along b - b' segment and a - a' segment. The lateral volume of the electromagnetic fields shrunk for smaller T_{th} . The field penetrates deeper into the sample for higher T_{th} . While small T_{th} gives higher spatial resolution, increasing T_{th} enhances subsurface imaging.

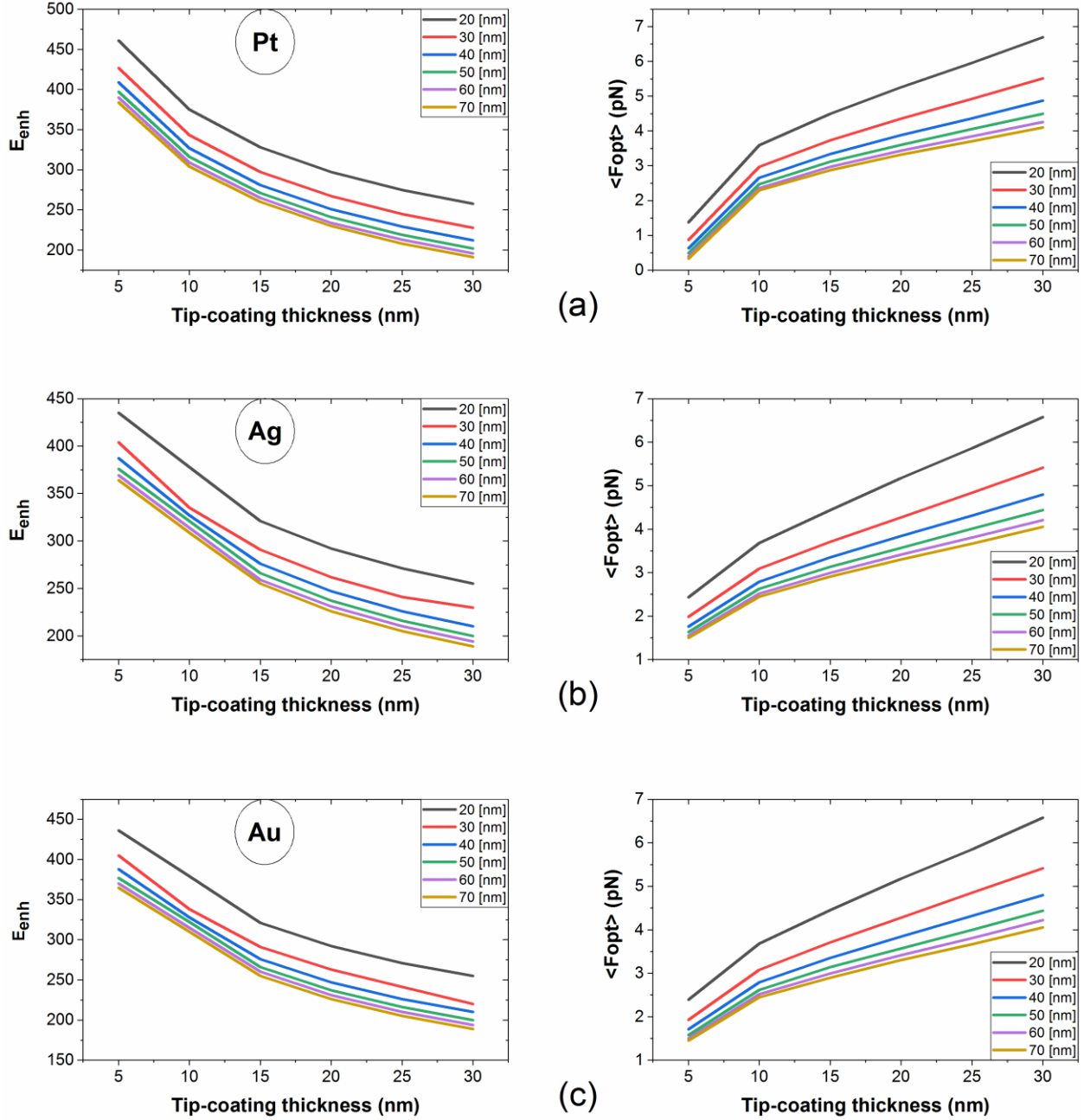


Fig. 5 Gap-field enhancement (E_{enh}) (left column) and $\langle F_{\text{opt}} \rangle$ (right column) as a function of T_{th} , where each curve represents specific S_{th} . (a), (b), and (c) correspond to different tip-coating materials: platinum (Pt), silver (Ag), and gold (Au). The incident wavelength is $10\mu\text{m}$. Reference [29].

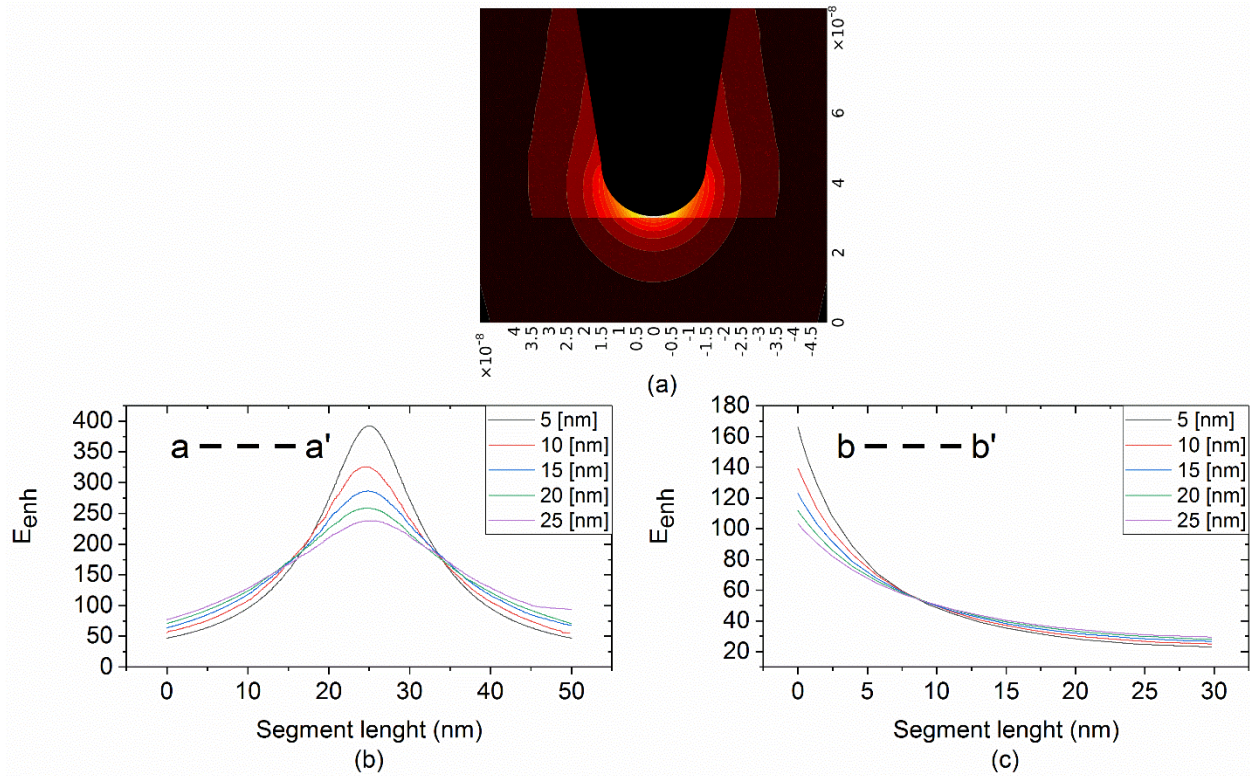


Fig. 6 (a) Near-field distribution is calculated at $T_{th} = 5$ nm. The spatial confinement of the electric field calculated through a - - a' segment (b) and vertically through b - - b' segment (c) (cf. Fig. 3(a)). Each color represents different T_{th} . S_{th} is 30 nm and the tip-coating material is Au. Reference [29].

2.3.6 Optical force spectrum at an absorption band

The gradient force spectrum over an absorption band, (in the electrostatic approximation), is dependent on the real part of the product of the tip and sample polarizabilities. Since the imaginary part of Au polarizability, in the IR region, is much smaller than the real part (the tip being assumed to be spheroid), the gradient force over an IR absorption band is dispersive (following the real part of the sample polarizability). In the visible region, however, both real and imaginary part of tip and sample

polarizability contribute to the gradient force. Fig. 3(a) was simulated to investigate the gradient force spectrum in IR absorption band. The sample materials were PMMA in one simulation and Polystyrene (PS) in another. The incident wavelengths covered the absorption band of PMMA at 1730 cm^{-1} and of PS at 700 cm^{-1} . Fig. 7(a) and Fig. 7(b) shows that the force spectrum takes a dispersive line shape, indicating that the gradient force predominantly follows the real part of sample polarizability.

In the above simulations, the PMMA and PS were assumed to be 30 nm thin film deposited on the Si substrate. The lateral dimensions were assumed to be infinite. To assess the gradient force spectrum in the visible, we impeded a 5 nm gold nanoparticle in the PMMA thin film (see Fig. 3(b)). Nanoparticle dielectric functions were used for the Au particle and bulk dielectric function were used for the tip. Interestingly, the spectrum of the gradient force shows three plasmon peaks; this can be explained by the hybridization effects^{43,44,45,46}. The tip can be assumed to be nanoshell. The spectrum of the gold nanoshell is governed by the interaction of the induced charges in the outer and inner interfaces of the Au nanoshell (tip coating layer). These induced charges when interact cause a split in the plasmonic resonance peak into two peaks. The lower energy peak corresponds to the charges that oscillate symmetrically (bonding) and the higher energy peak corresponds to the charges that oscillate anti-symmetrically (antibonding). Under weak interaction, the gap between these oscillation energies is negligible producing one plasmon peak. However, this gap increases under strong interaction, leading to two plasmon peaks. The third plasmon peak located as a higher energy and that is attributed to the particle plasmon Fig. 7(c), shows that the force spectrum is absorptive.

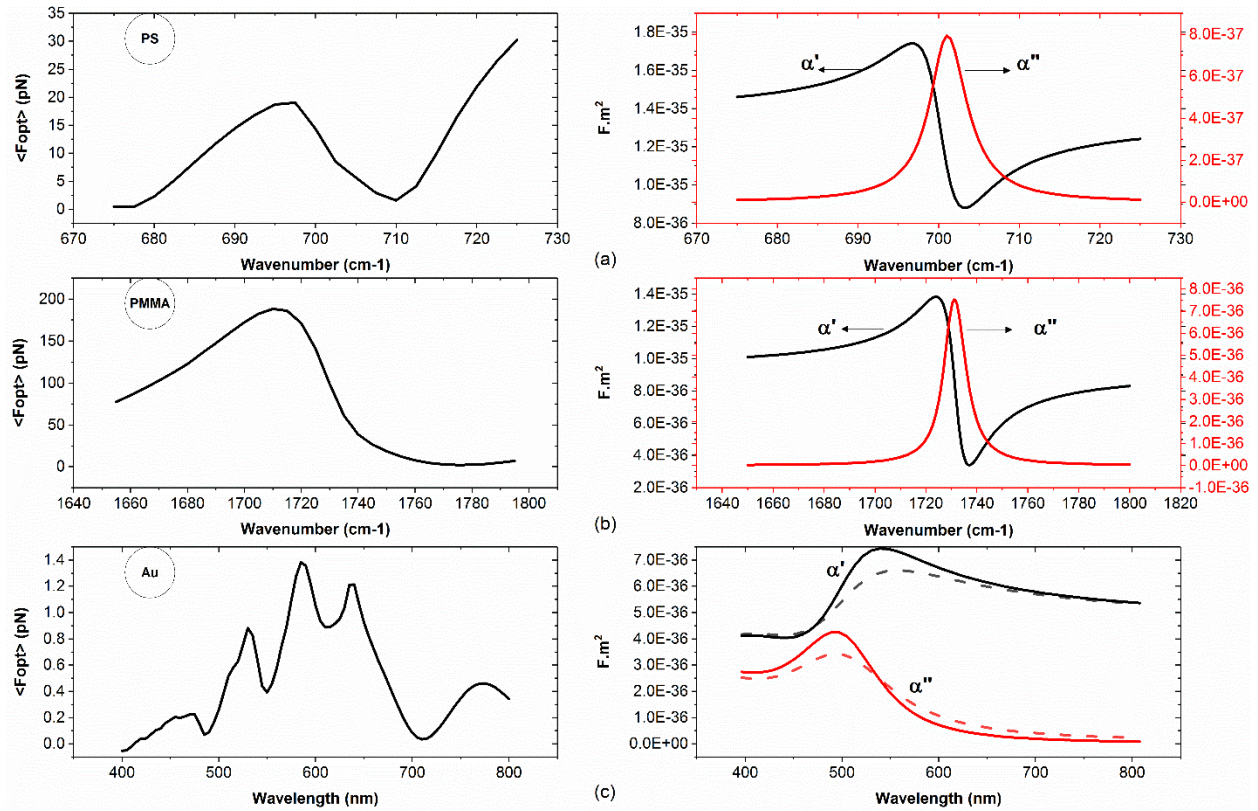


Fig. 7(a) $\langle F_{opt} \rangle$ as a function of PMMA absorption band (left) and the real (α') and imaginary (α'') parts of PMMA polarizability (right). (b) $\langle F_{opt} \rangle$ as a function of PS absorption band (left), and α' and α'' parts of PS polarizability (right). (c) $\langle F_{opt} \rangle$ calculated in the visible region for Au (left), and α' and α'' parts of Au polarizability (right); the bulk Au polarizability is drawn in solid, and nanoparticle Au polarizability is drawn in dashed line. Reference [29].

2.3.7 Lateral, subsurface, and spectral imaging performance

To assess the lateral and subsurface imaging capabilities of the PiFM, particle with 5 nm radius is impeded in PMMA thin film and scanned laterally and vertically as illustrated in Fig. 3(b). two materials will be used for the particle: Au and PS. The

excitation wavelength is at the optical resonance of Au particle $\lambda = 530$ nm, and, in a separate simulation, a PS particle is excited at the absorption band of 700 cm^{-1} . The averaged optical force on the tip is calculated using Eq. (23) as a function of particle position. Fig. 8 shows that the forces sensed by the tip decrease exponentially as the particle is swept vertically, i.e., into the PMMA. The rate of decrease is dependent on the tip radius and the excitation wavelength of the beam, i.e., as the particle is swept deeper into the PMMA thin film, the force decreases with a slower rate in the IR than in the visible. In both cases (Au and PS), the calculated force induced by the particle is in the pN range. Lastly, the particle was swept laterally at different vertical depths (i.e. at $d = 0, 2, 5$ nm, and 10 nm see Fig. 3) to study the contrast defined as $\mathbf{F}_{\text{cont}} = \langle \mathbf{F}_{\text{opt}} \rangle - \langle \mathbf{F}_{\text{opt, min}} \rangle$. Fig. 8(c) shows that at depth $d = 5$ nm, the Au particle contrast disappears, which is attributed to the rapid electric field gradient. For PS particle, the field gradient is smaller leading to a measurable contrast even near $d = 5$ nm (Fig. 8(d)). Therefore, IR-PiFM subsurface imaging capability is superior.

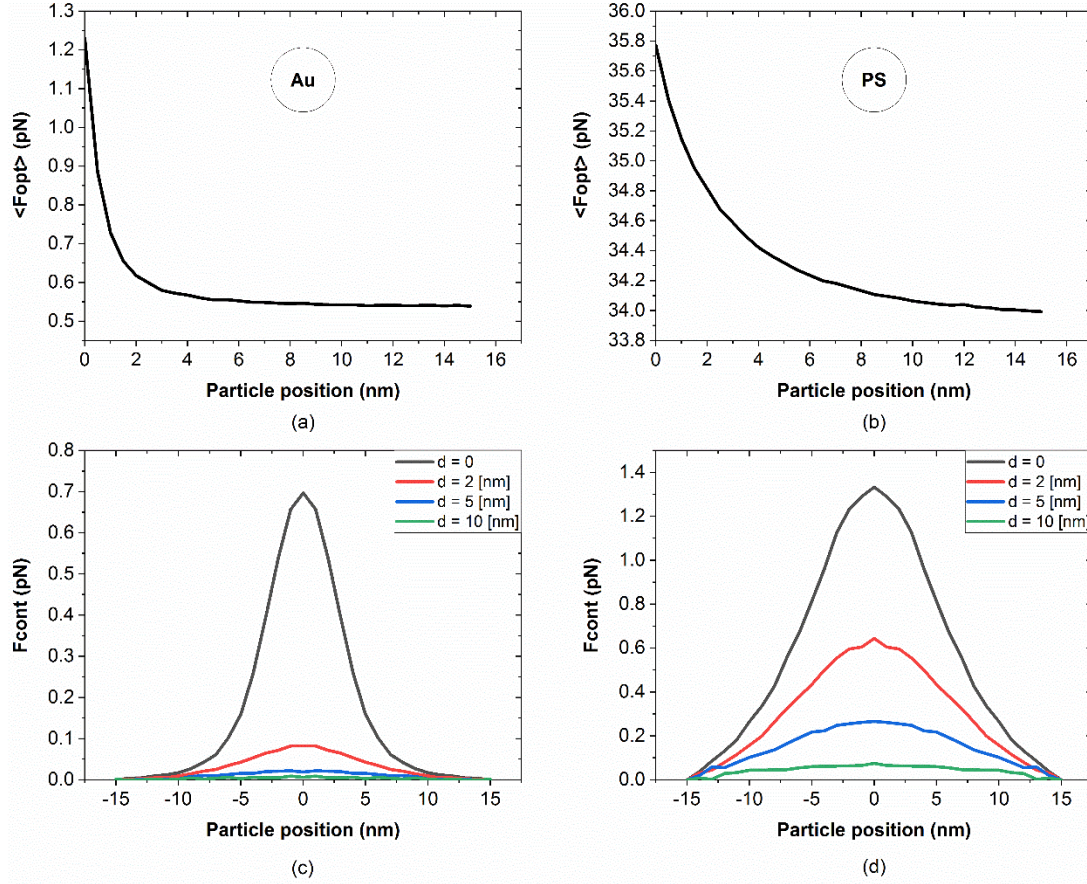


Fig. 8 (a) and (b) are the $\langle F_{opt} \rangle$ calculated as a function of particle depth d (direction 2 (cf. Fig. 1(b))). (c) and (d) are $\langle F_{cont} \rangle$ calculated while the particle is swept in direction 1 for different depths d . The particles are excited at resonance. Reference [29].

Spectral imaging performance is assessed by deriving the particle ON and OFF its optical resonance. The dielectric function is tabulated in Table. 1. In both cases, the particle location is swept laterally and $\langle F_{cont} \rangle$ will be calculated. The averaged optical force that is used to assess the spectral performance is defined as $\langle F_{spec} \rangle = \langle F_{opt,ON} \rangle - \langle F_{opt,OFF} \rangle$, where $\langle F_{opt,ON} \rangle$ and $\langle F_{opt,OFF} \rangle$ are optical force calculated when the particle is excited ON and OFF optical resonance respectively. This has been demonstrated for PS, Au, and SiC particles in Fig. 9. The figure shows that at resonance the tip feels a

stronger force than off resonance. Surprisingly, although the particle volume is very small the force difference between ON and OFF resonance is in the order of 0.75 pN for the PS particle, 0.7 pN for the Au particle, and 20 pN for SiC particle. Three reasons why the force difference is expected to be low. First, the particle volume is very small; the particle radius is only 5 nm. Second, the particle is impeded in a dielectric thin film of refractive index $n = 1.54$. Therefore, the electric field at the particle surface is lowered by 1.54. Third, the particle is 20 nm from the Si substrate; this means that the local field enhancement that derive the particle is much lower than if the particle directly set on the substrate. If the particle set on the Si substrate and the thin film is removed, the optical force at 0.5 nm spacing is expected to be larger.

Table 1: Dielectric functions used to find $\langle F_{\text{cont}} \rangle$ for ON and OFF resonance.

	Au		PS		SiC	
	ON lda= 585nm	OFF lda= 680nm	ON lda=14.28um	OFF lda=16um	ON lda=12.6um	OFF lda=16um
n + ik	Bulk 0.68+2.015i	Bulk 0.17+3.7i	1.65+0.04i	1.57+0.002i	17+17i	17
	Nanoparticle 0.89+2.07i	Nanoparticle 0.58+3.7i				

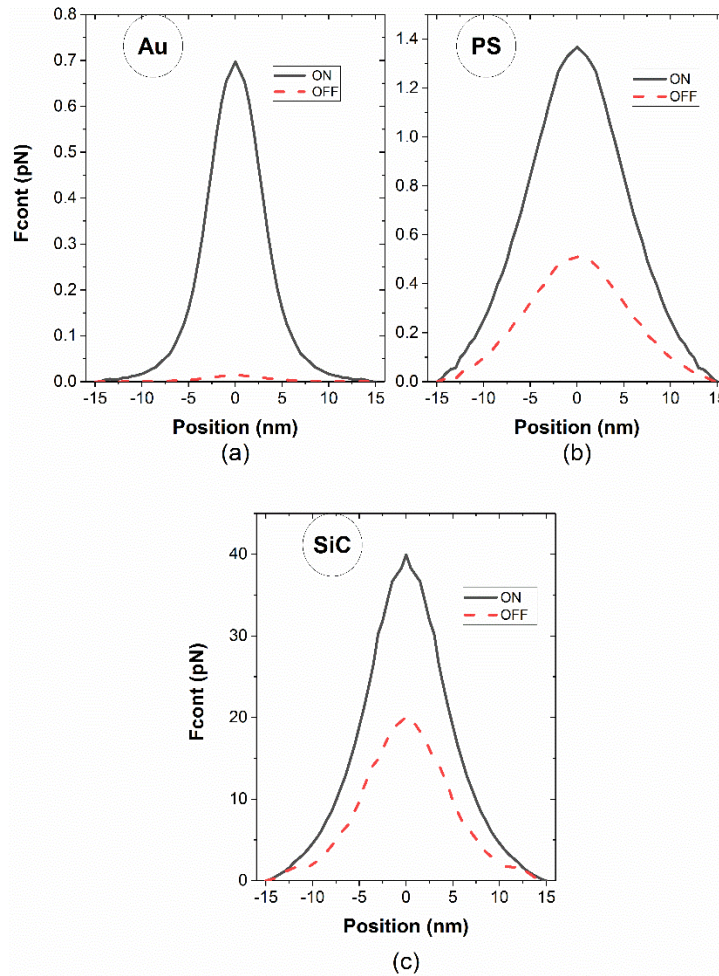


Fig. 9 F_{cont} at on optical resonance (solid red line) and off optical resonance (dashed red line) conditions for Au (a), PS (b), SiC (c). Reference [29].

2.3.8 Discussion

In earlier work, the tip and sample have been modeled as two spheres separated by 1 nm gap²⁶. They show that the gradient force, in this case, is in fN range. However, gap-field enhancement will be significantly underestimated if substrate and lightning rod effects are excluded⁴⁷. This, in turn, lowers the calculated optical forces by orders of magnitude. The substrate effect on E_{enh} is clear as shown in Fig. 5.

Photoinduced forces between tip-sample have been demonstrated for the visible and IR regions. The mechanical action of the near-field optical interaction is clear, and it depends locally on the sample polarizability. However, the argument is about the origin of this force. Gradient force, van der Waals mediated thermal expansion, and short-range thermal expansion were proposed, in separate studies^{27,32}, as the origin mechanism of the measured photoinduced force. The numerical simulation shows that gradient forces are indeed in the detectable pN range even for sample particle with 5 nm radius. However, the spectral line shape of the gradient forces shows a distorted dispersive curve. This contradicts the measured photoinduced forces of polymers in the IR region.

2.3.9 Conclusion

Modelling the tip and sample by two interacting spheres excludes the effect of the substrate as well as the lightning rod effect. The absence of these effects underestimates the gap-field enhancement which in turn reduces optical forces by orders of magnitudes. Moreover, the tip-coating thickness effect must also be considered; the enhancement reduction as coating thickness increases to 35nm is roughly 40%. In the IR, coating the tip with Pt, Au, or Ag does not make a significant difference on the gap-field enhancement. Force behavior has been assessed over absorption bands, and the results show dispersive behavior at PS and PMMA absorption bands, namely 700cm^{-1} and 1730cm^{-1} respectively. However, force behavior is absorptive when Au particle is interacting with the tip over the visible region. Numerically, near-field optical forces developed in the vicinity of the tip apex due to tip-

sample optical interactions is shown to be detectable and in the pN range. PiFM allows embedded particles to be imaged laterally with higher spatial resolution in the visible region than in the IR, ascribed to the spatial confinement of the gap-field enhancement at the tip. Vertical imaging range is increased using IR excitation, as the gradient force is less steep than in the visible. In addition, increasing tip coating thickness allows electric fields to penetrate deeper into the sample, which further enhances the subsurface imaging range.

2.4 Nanoscale Opto-Mechanical Molecular Damping as the Origin of Spectroscopic Contrast in Photo Induced Force Microscopy

2.4.1 Introduction:

The integration of atomic force microscopy (AFM) with focused lasers has enabled nano-chemical imaging and spectroscopy with spatial resolution well beyond the diffraction limit. One classic example is apertureless near-field scanning optical microscopy (a-NSOM or sSNOM)^{5,6,48,49}. In this method, the enhanced optical field of the scanned AFM probe is perturbed by the local near-field generated by the excited sample, and the scattered near-field (amplitude and phase) is detected in the far-field using an interferometer to record the image. Photothermal induced resonance (PTIR)^{50,51} and peak force infrared (PFIR)⁵² are two examples for characterizing sample chemical properties based on AFM. In these techniques, the sample thermal expansion induced by optical absorption is detected using an AFM tip in contact. An alternative, noninvasive microscopy and spectroscopy technique that has emerged recently is photoinduced force microscopy (PiFM)²⁴ (Fig. 10). In this method, the tip-sample optical interaction is measured with the AFM operating in non-contact mode. The topography is recorded using the 2nd mechanical eigenmode of the cantilever at f_2 . A quantum cascade laser (QCL) is amplitude modulated at f_m (where $f_m = f_2 - f_1$) and focused on the tip end, and the opto-mechanical response is measured at the 1st mechanical eigenmode at f_1 . Many applications of PiFM have emerged. Near-field electromagnetic field characterization^{33,53–57}, nonlinear optical measurements such as Raman⁵⁸

spectroscopy and stimulated Raman spectroscopy^{59,60}, time-resolved pump-probe microscopy⁶¹, organic solar cells studies⁶², optical phonon polariton imaging and nanoscale chemical imaging in the mid-infrared²⁵ are but a few examples.

While the dipole-dipole force model provides excellent agreement with the electromagnetic near field measurements in the visible⁶³ and with mid-infrared plasmonic resonance spectra⁶⁴, extending this model to infrared vibrational resonances causes discrepancies between experiment and theory^{25,29,65}. In particular, the dipole-dipole force model predicts a dispersive spectral response, while the experimental results show a purely dissipative response. Three alternative proposals for explaining PiFM spectroscopic contrast in the infrared have been proposed to address this discrepancy. They are (1) detecting photothermal expansion using short range repulsive forces acting on the AFM cantilever/tip^{26,27} in contact (2) detecting photoacoustic pressure waves generated at the sample surface resulting in long range repulsive forces acting on the cantilever/tip²⁷ (3) detecting van der Waal mediated force modulation caused by sample thermal expansion³².

In this paper, we report on a series of experiments aimed at unravelling the origin of PiFM spectroscopic contrast in the infrared. Our experimental findings support the hypothesis that the spectroscopic contrast in PiFM is mediated by opto-mechanical damping of the cantilever oscillation as the optical wavelength is scanned through optical resonance. Here, the rate of dissipated mechanical power due to interactions induced by tip-sample dissipation processes can be divided into three components; Γ_{ts} due to adhesion, viscous damping, etc., Γ_c due to air or fluid damping and Γ_{opt} due to

opto mechanical damping driven by dissipative near-field optical interaction. In our analysis we assume that the opto-mechanical damping constant can be described by a velocity dependent term. The effective damping constant (Γ_{eff}) includes all damping effects ($\Gamma_{\text{eff}} = \Gamma_{\text{ts}} + \Gamma_{\text{c}} + \Gamma_{\text{opt}}$), i.e., the total mechanical power dissipation increases upon optical absorption. We hypothesize that opto-mechanical damping force (change in energy with respect to distance) is caused by the excited sample molecules creating a dissipative force on the vibrating tip. We show that this contrast mechanism provides an excellent match with the experimental results. The theory can be extended to the single monolayer detection limit.

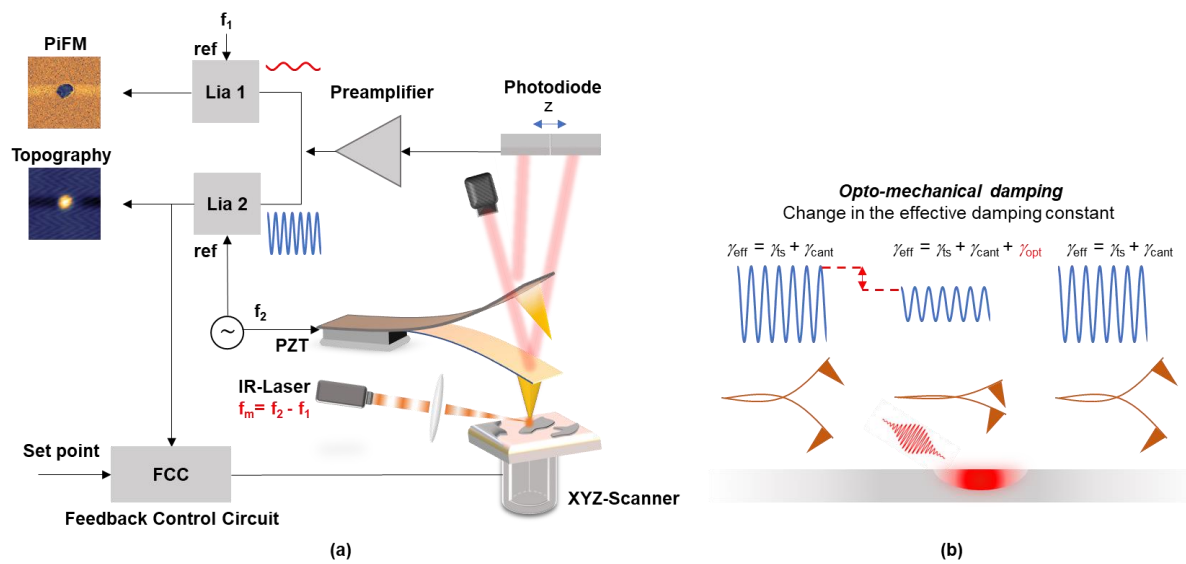


Fig. 10 Schematic of IR PiFM experiment and principle of opto-mechanical damping. **a** The cantilever is mechanically vibrated at its 2nd mechanical eigenmode f_2 , so that peak-peak oscillation is 6 nm. Lock-in amplifier and feedback laser position sensitive detector (PSD) are used to stabilize the cantilever nanometers from sample surface. The IR source is electrically triggered at $f_m = f_2 - f_1$, where f_1 is the 1st mechanical eigenmode of the cantilever. The incident infrared pulse is p-polarized (along the tip axis) and focused

to 20-um-diameter spot. The topography and the PiFM signals are simultaneously recorded at f_2 and f_1 respectively. The image is generated via raster-scanning the sample under the tip. **b** illustrates the principle of opto-mechanical damping, where oscillation amplitude is damped due to IR vibrational resonance. Reference [30].

2.4.2 Distinguishing Between Repulsive and Attractive Optical Forces

The near-field gradient forces acting on the tip-apex modify the cantilever compliance or stiffness (k). This change in k is measured as a frequency shift in the mechanical resonance of the cantilever. Mathematically, the cantilever resonance is defined as $\omega = \omega_0 \pm (\nabla F/m)^{0.5}$, where m is the effective mass of the cantilever and ∇F is the force gradient and ∇ is the gradient operator. Depending on the sign of ∇F , the cantilever resonance shift to higher or lower values. The shift to higher values indicates repulsive interactions, and the interaction is attractive if the frequency shifts to lower values. Here the photoinduced force was examined by recording the frequency shift of f_1 as the excitation wavelength is tuned across a PS resonance at 1494 cm^{-1} ; the tip-sample gap is controlled at f_2 , and the PiFM was operating in heterodyne mode. Fig. 11 shows f_1 shift as a function of excitation wavelength and the point spectrum of the PS thin film as a reference. The sample is 60 nm thick polystyrene (PS) film on gold (Au) substrate. Relative to off resonance excitation, f_1 shifts to lower values on resonance, revealing the attractive nature of the photoinduced force. Previous works⁶⁶ have also come to the same conclusion, but with different approach. The measured frequency shifts were about 400 Hz. We conclude that short-range thermal expansion forces in contact

(repulsive forces) and photoacoustic long range repulsive forces are not relevant in PiFM when operating in heterodyne mode.

When PiFM is operated in direct mode, however, photoacoustics exert a global repulsive force on the cantilever. While the cantilever is lifted 3 μm from sample surface, we were indeed able to detect a global photoacoustic effect originating from the focused infrared beam for relatively thick samples ($> 100 \text{ nm}$) see Fig. 12. The figure also shows that the photoacoustic forces significantly damped when operating in a rough vacuum of 0.3 torr.

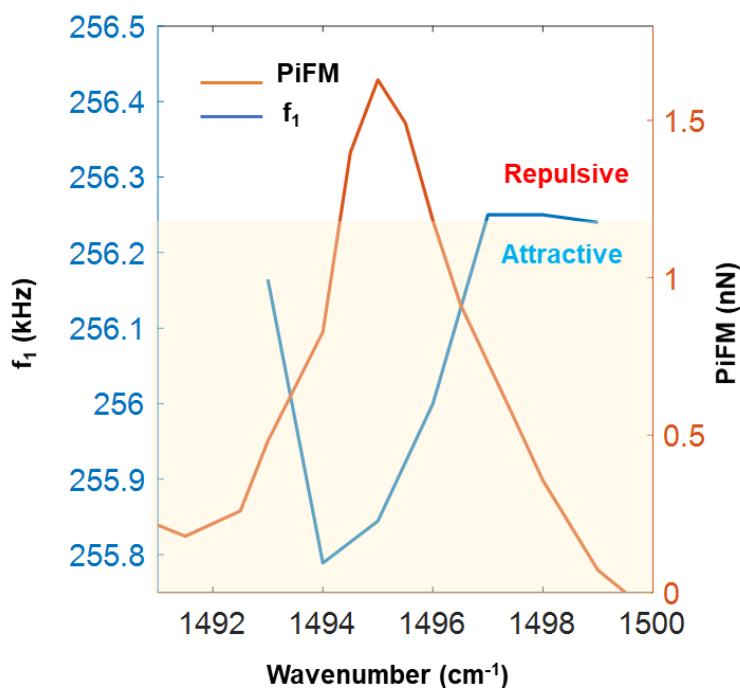


Fig. 11 Cantilever frequency shift across an absorption band. Shift of the cantilever resonance frequency at f_1 (blue line) across PS absorption band at 1495 cm^{-1} (Orange line). The sample is 60 nm thick PS film on Au substrate. Input average power was 1 mW focused to 20- μm -diameter spot. Reference [30].

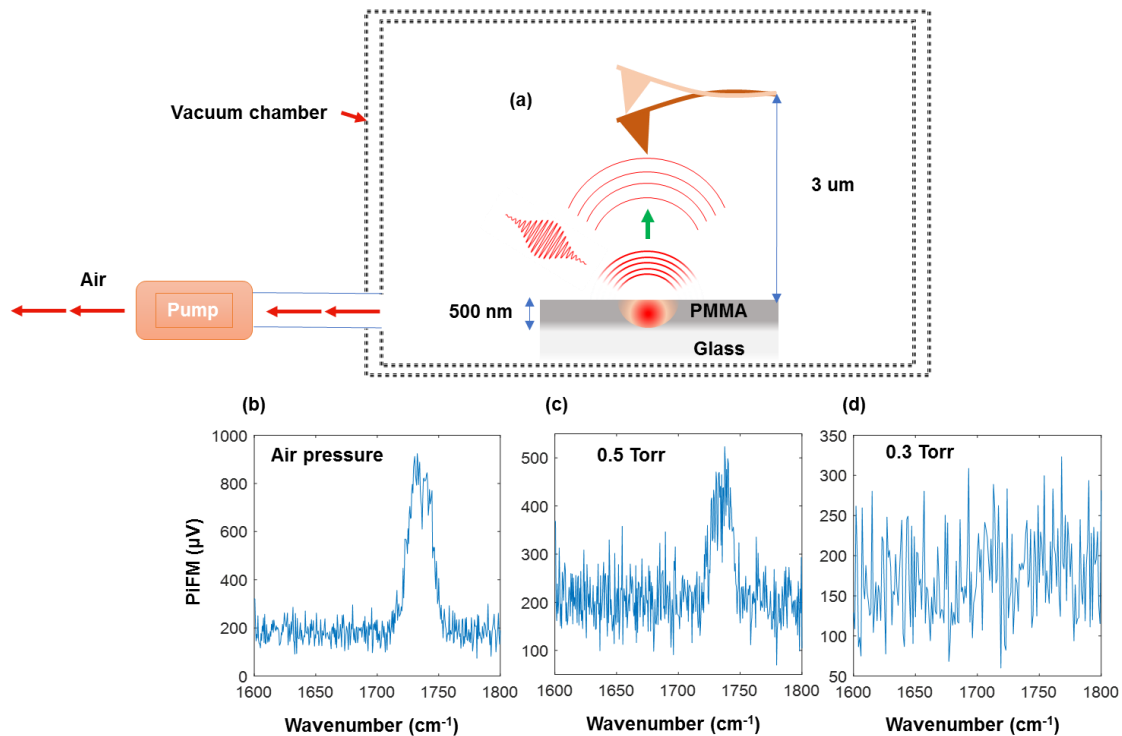


Fig. 12 Measurement of gas photo-acoustic waves while tip is retracted from sample by 3 μm . a 500 nm thick PMMA was excited by infrared laser source modulated at $f_m = f_1$ (direct PiFM mode), where tip-sample distance is about 3 μm . The tip-sample system were enclosed in a vacuum chamber and an air pump is used to decrease pressure. b-d Photoacoustic signals at 1.7 Torr, 0.5 Torr, and 0.3 Torr respectively. Reference [30].

2.4.3 Piezo Vibration Experiments and PiFM Sensitivity to Thermal Expansion

When sample is excited on optical vibrational resonance some of the incident power is absorbed and converted into heat. This induces thermal expansion that could change the strength of the local van der Waals forces and its gradient sensed by the cantilever tip; this force is named as van der Waals mediated thermal expansion F_{vdW}^{th} . When light is modulated, F_{vdW}^{th} and its gradient ∇F_{vdW}^{th} is modulated. This effect was proposed by Potma and coworkers³² as a contrast mechanism for PiFM when exciting optical vibrational resonance in midinfrared. Here, F_{vdW}^{th} was mimicked using a vibrating PZT crystal that was independently calibrated using heterodyne laser interferometer (see Fig. 13). Experiments were carried out to determining the smallest detectable thermal expansion in our PiFM.

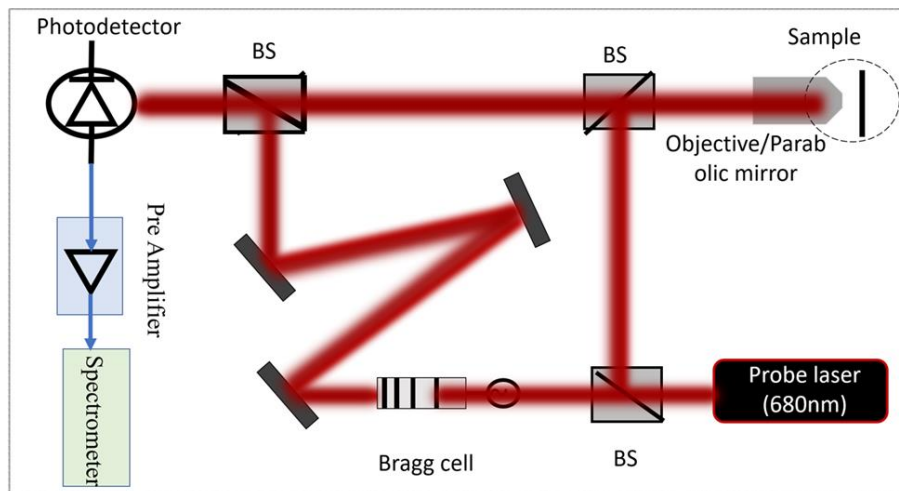


Fig. 13 Interferometric setup for calibrating the PZT Crystal. Reference [30].

Fig. 14 (b) depicts our experimental set up. Once the tip was stabilized nanometers from the template-stripped gold (TSG) attached to the PZT, a sinusoidal signal was applied to the PZT to vibrate it at $f_m = f_2 - f_1$. The F_{vdW}^{th} and ∇F_{vdW}^{th} were modulated at f_m due to the PZT because the effective tip-sample spacing was changing at f_m . In principle, A_2 is amplitude modulated due to ∇F_{vdW}^{th} not F_{vdW}^{th} . The modulated vdW at f_m mixes with f_2 to generate a signal at f_1 due to nonlinear tip-sample interactions. We plotted the sensitivity (S) defined as the ratio of the measured signal (cantilever deflection in pm peak-peak) to the piezo displacement (pm) and compared it with the noise level of the PiFM to determine the minimum detectable thermal expansion. Results in Fig. 14 (a) show a linear relationship between PZT displacement and the observed signal, with $S = A_1/d = 1$ pm/pm, where A_1 is the peak-peak oscillation amplitude of f_1 and d is the PZT displacement. Since the noise level measured at f_1 is about 32 pm for 5 ms integration time (orange line in Fig. 14) thermal expansion below 32 pm will not be detectable in our system. In previous work, thermal expansion for a 60 nm PS film on silicon substrate (excited at 1452 cm^{-1} with 5 mW average power focused to 20 μm diameter spot) has been calculated to be about 30 pm, which is already below our noise level³². Samples with monolayer thickness, under similar conditions, expand to a few pm only²². Thus, if the heterodyne PiFM measures thermal expansion, monolayer sample cannot be detected. In the following section, the response of a 4-methylbenzenethiol (4-MBT) monolayer on TSG was measured, further confirming that our PiFM contrast cannot be thermal or F_{vdW}^{th} in origin.

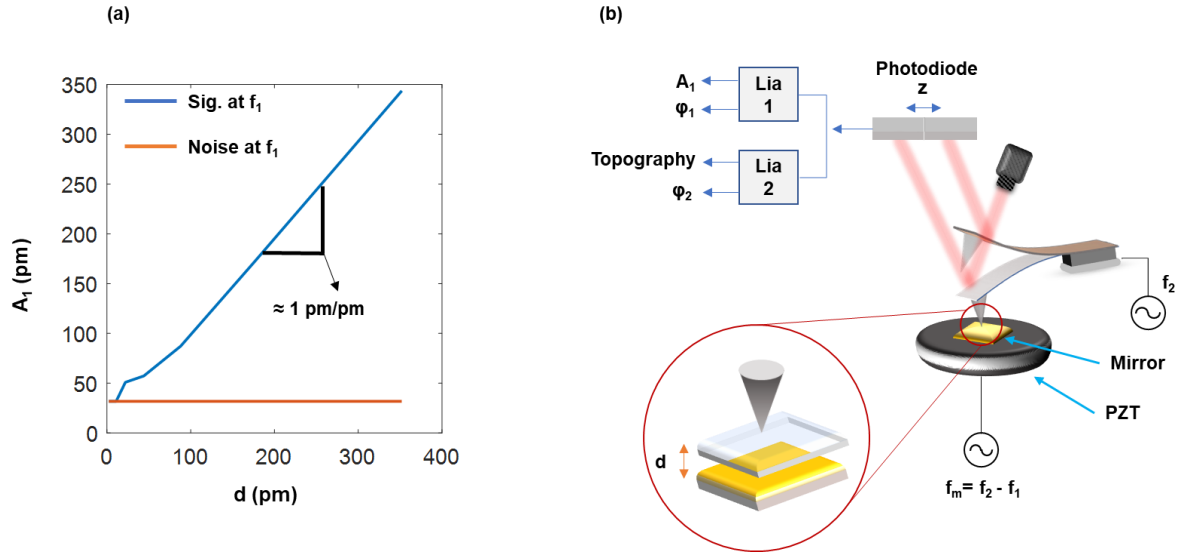


Fig. 14 Non-contact AFM sensitivity to thermal expansion. **a** The peak-peak oscillation amplitude (blue solid line) measured at f_1 as a function of the PZT displacement amplitude (d). The noise level of the system measured at f_1 corresponds to oscillation of about 50 pm peak-peak as indicated by the orange line. Tip-sample gap is controlled at f_2 and the PZT is driven at $f_m = f_2 - f_1$. **b** depicts the experimental setup. Reference [30].

2.4.4 Monolayer PiFM Experiments

4-MBT on TSG was prepared by immersing the TSG in the 4-MBT solution overnight. To demonstrate PiFM sensitivity to optical forces generated by a monolayer-thick sample, the 4-MBT was excited at molecular vibrational resonances. To generate gold islands as seen in the figure, the TSG is sonicated in ethanol till gold start lifting off. The sample was excited with the exact same conditions as stated in Fig. 10, but with input averaged power of only 0.5 mW. The tip-sample gap was controlled at f_2 with A_2 of 6 nm peak to peak.

Fig. 15 shows the absorption spectrum of 4-MBT centered at 1495 cm^{-1} . Note that the peak-peak oscillation amplitude induced by the 4-MBT molecular resonance is about 392 pm. Giving $S = 1\text{ pm/pm}$, the monolayer must expand 392 pm. This expansion implies heating the sample by 100s degree. Thus, it is highly unlikely that the PiFM signal were induced by modulated thermal expansion. For example, under similar experimental conditions, thermal expansion of a monolayer has been calculated numerically to be $< 3\text{ pm}$ with a temperature increase of $< 6\text{ degrees}$ ^{22,67}. Here, if we assume the 4-MBT is 1 nm thick with linear thermal expansion coefficient of 10^{-4} [1/K] , and assume the sample was heated by 5° , then the sample would expand by 0.5 pm. This expansion is 64x smaller than the minimum detectable thermal expansion in our system, according to the PZT experiment. Fig. 15 c-e, respectively, show, topography, PiFM image when sample excited on resonance, and PiFM image when sample excited off resonance. We conclude that the observed PiFM signal clearly could not originate from $F_{\text{vdW}}^{\text{th}}$. The findings also support the fact that any $F_{\text{vdW}}^{\text{th}}$ effect on the PiFM signal is negligible. In what follow, experiments were performed to study the effect of vibrational resonances on the cantilever dynamics and to unravel the actual contrast mechanism in IR-PiFM.

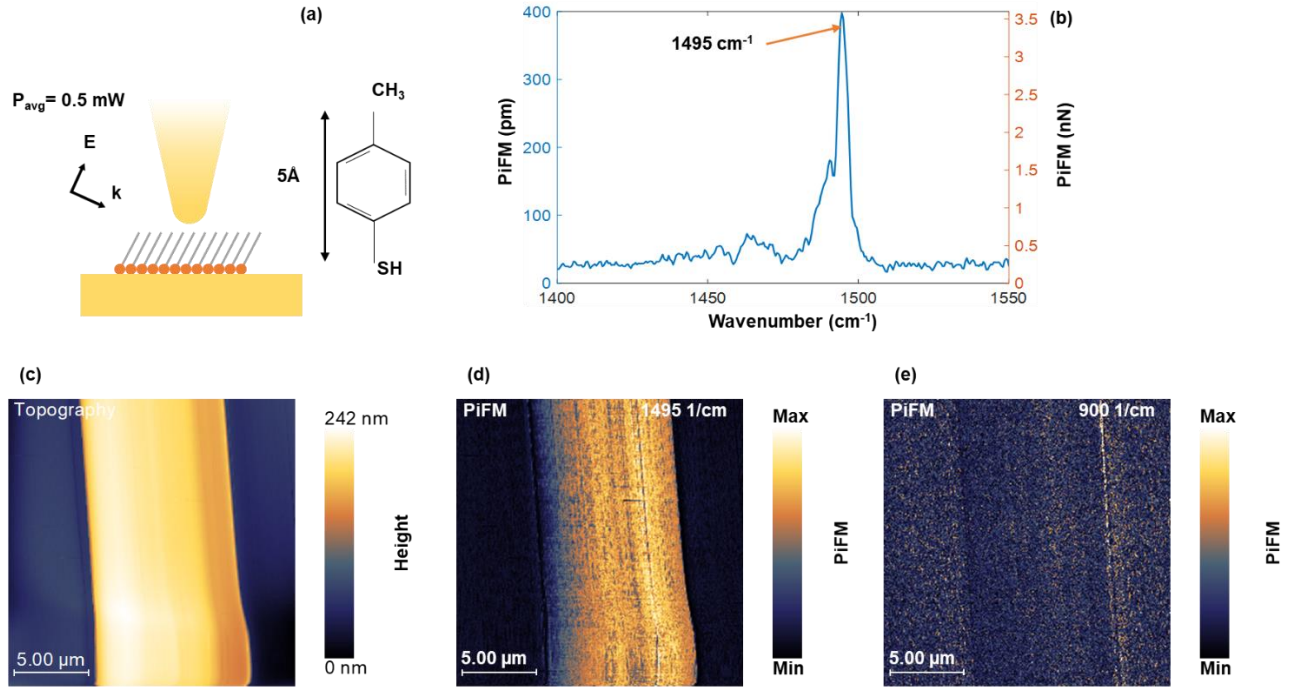


Fig. 15 Monolayer response. **a** is 4-MBT adsorbed on template-stripped gold. Excitation average power is 0.5 mW focused to 20-um-diameter spot. **b** is point spectrum of 4-MBT showing resonance at 1495 cm^{-1} . **c – e** are topography of gold island, PiFM image at 1495 cm^{-1} , and PiFM image off resonance respectively. Reference [30].

2.4.5 Opto-mechanical damping

The sidebands in PiFM can originate from either amplitude modulation (AM) or frequency modulation (FM) of f_2 . If the induced optical forces modify the effective stiffness of the cantilever, then we have FM. On the other hand, if the optical forces modify the effective damping constant Γ_{eff} , then we have AM. Once the modification of k_{eff} or Γ_{eff} is modulated at f_m , then sidebands is generated at $f_2 \pm f_m$.

Series of experiments were conducted to determine the origin of the sidebands signals detected in the standard heterodyne PiFM. First, the relative phase of the PiFM signal at f_1 is measured when the tip is excited slightly above f_2 (f_{2R}) and slightly below f_2 (f_{2L}). This relative phase is defined as $\varphi_{\text{rel}} = |\varphi_1^{f_{2R}} - \varphi_1^{f_{2L}}|$. If optical forces are conservative and attractive, A_2 will decrease, for f_{2R} case, and increase, for f_{2L} case. Because the induced change in A_2 is opposite in these two cases φ_{rel} is expected to be about 180° out of phase. Note that f_2 is used to control tip-sample gap. The sample was 60 nm PMMA on glass. The laser excitation wavelength was tuned to a PMMA resonance and the laser was modulated at $f_m = f_2 - f_1$. As illustrated in Fig. 16, If the optical force is dissipative, A_2 will decrease for both cases. This means that φ_{rel} is about 0° . This is illustrated in Fig. 16 a-d Thus, φ_{rel} can be used to understand the nature of the interaction. The measured φ_{rel} using a lock-in amplifier was nearly 0° see Fig. 16 e-f indicating that our PiFM signal contrast was originating from AM rather than FM modulation of f_2 .

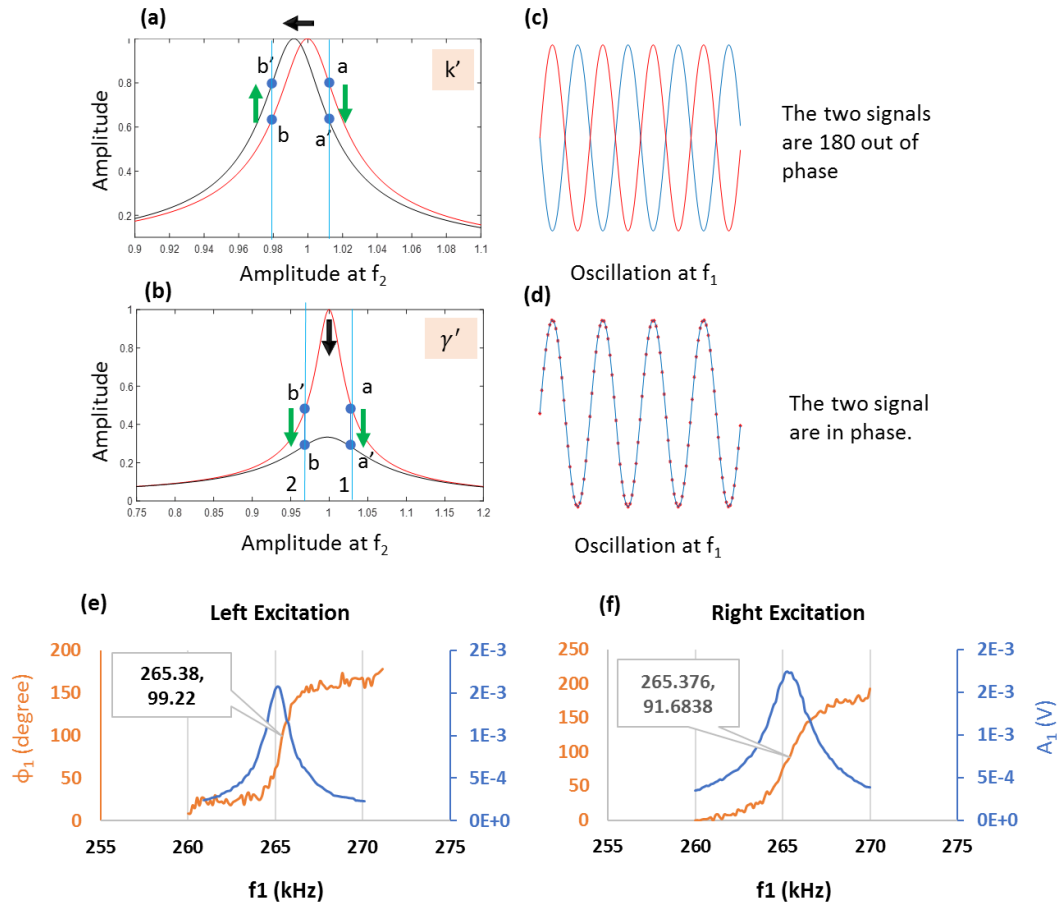


Fig. 16 Phase measurement comparison between left and right excitation. Amplitude change of the 2nd mechanical mode due to conservative a and dissipative b interactions. The expected relative phase between f_{2R} (a-a') and f_{2L} (b-b') excitations, measured at the 1st mechanical mode is shown in c and d. Phase measurement of the 1st mechanical mode for left excitation e and right excitation f. The phase and amplitude are measured using lock-in amplifier. Reference [30].

The finding has been confirmed by directly measuring the change in A_2 , while the tip is engaged with the sample (PMMA), as we tuned the excitation wavelength across PMMA absorption band. Here the feedback loop was open, and the excitation

wavelength was tuned rapidly across the PMMA absorption band. The change in A_2 was recorded for f_{2R} and f_{2L} as shown in Fig. 18 d and f. The acquisition time was fast to avoid artifact induced by thermal drift and the laser was modulated at $f_m = 1$ MHz, far from f_2 and f_1 (see Fig. 17). In other words, the cantilever was oscillating at f_2 only and the laser acted as a CW source. Our experiments revealed that A_2 was damped for both cases, and the damping is wavelength dependent and follows closely the PMMA spectrum (shown in orange as a reference).

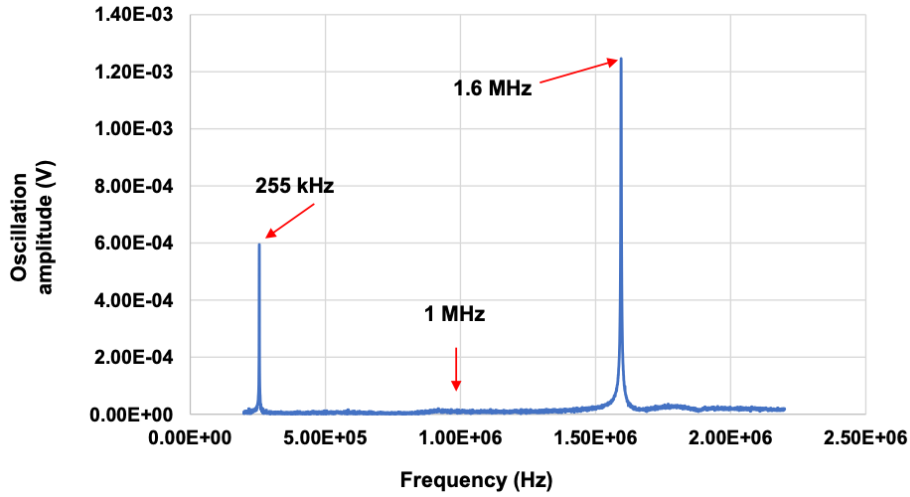


Fig. 17 1st and 2nd mechanical modes of the cantilever used in this paper. Note that at 1 MHz there is no cantilever oscillation, and $f_2 - f_m$ does not overlap with f_1 . Reference [30].

In dynamic AFM, the phase of the oscillating cantilever near sample surface can be

$$\varphi = -\sin^{-1}\left(\frac{A_s}{A_2} * \left[\frac{\langle P_{diss}^{ts} \rangle}{\langle P_{diss}^c \rangle} + 1\right]\right) \quad (26)$$

written as

Where $\langle P_{\text{diss}}^{ts} \rangle$ is the averaged power dissipated by tip due to the sample effect, $\langle P_{\text{diss}}^c \rangle$ is the averaged dissipated energy induced by air damping and cantilever intrinsic losses, A_0 is the oscillating amplitude when cantilever is engaged with the sample, and A_2 is the free oscillating amplitude. We call the ratio A_0/A_2 the set point. Note that if the optical interactions are purely conservative, i.e., $\langle P_{\text{diss}}^{ts} \rangle = 0$, then the phase closely follows the setpoint, and because the setpoint is always maintained to be fixed, the phase also remain fixed. On the other hand, if the optical interactions are dissipative, then we should see a change that is wavelength dependent and closely follow the sample vibrational resonance. Here, we have engaged with the sample using heterodyne PiFM and tuned the excitations wavelength across the PMMA absorption band (1733 cm^{-1}) and recorded φ_2 . As expected from dissipative interactions, φ_2 decrease for f_{2R} and increases for f_{2L} and follows closely the PMMA spectrum see Fig. 18 a, c, and e.

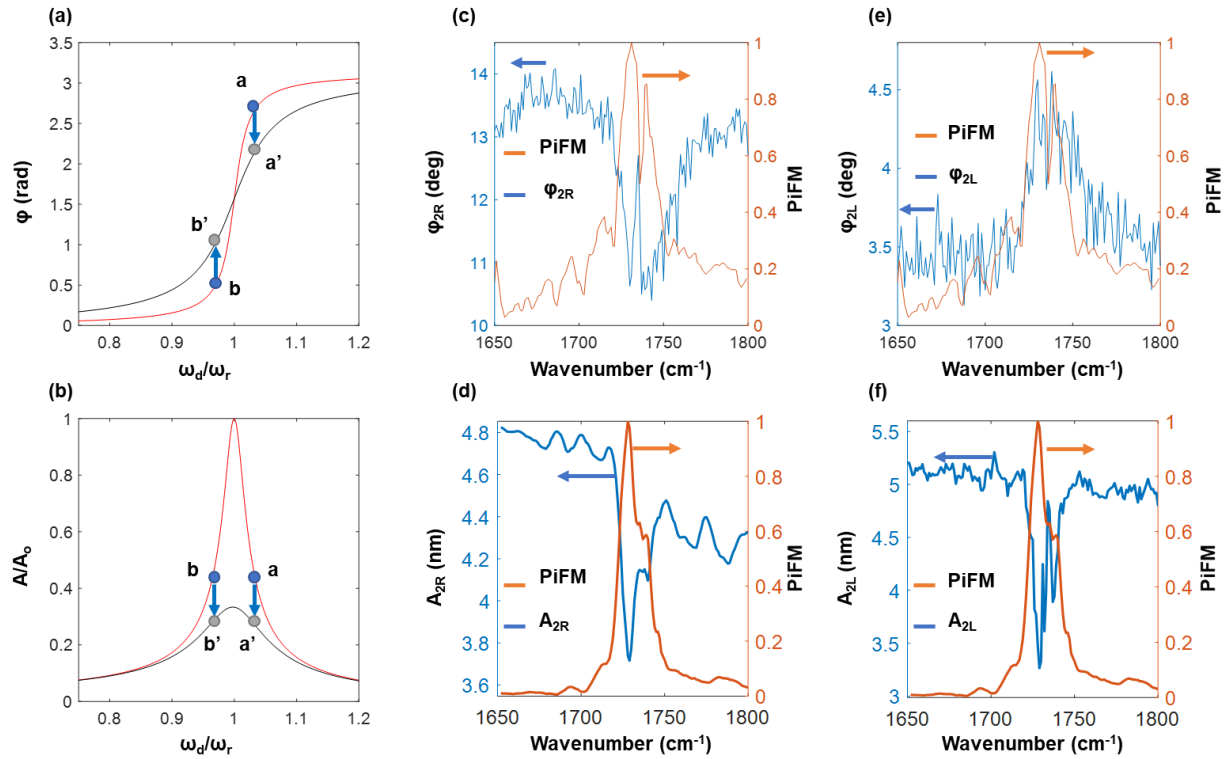


Fig. 18 Opto-mechanical damping. a and b are phase and amplitude of high Q (red) and low Q (black) harmonic oscillator. Change in the phase (ϕ_2) and amplitude (A_2) of the 2nd mechanical mode (blue line) across PMMA absorption band (orange line) centered at 1733 cm⁻¹ for right excitation **c** and **d** and left excitation **e** and **f**. Sample is 60 nm thick PMMA on glass. The phase measurements were conducted using standard PiFM mixing mode, while amplitude measurements were conducted with the feedback loop open and the wavenumber scanned rapidly through resonance as explained in the text. Reference [30].

Based on all our experiments, we conclude that the optical forces are mainly dissipative and the change in the effective damping constant is the origin of the side bands signal detected at f_1 . Thus, f_2 is mainly amplitude modulated not frequency modulated. The

finding clearly suggests that the optomechanical damping follows the imaginary part of the complex refractive index.

The change in A_2 and ϕ_2 can be understood by adding linearly the optomechanical damping to the total energy dissipated. Thus Eq (18) and Eq. (26) can be written as

$$A_0 = A_2 \sin(\phi) \left(\frac{\langle P_{\text{diss}}^{\text{ts}} \rangle + \langle P_{\text{diss}}^{\text{opt}} \rangle}{\langle P_{\text{diss}}^{\text{c}} \rangle} + 1 \right)^{-1} \quad (27)$$

$$\phi = \sin^{-1} \left(\frac{A_0}{A_2} * \left[\frac{\langle P_{\text{diss}}^{\text{ts}} \rangle + \langle P_{\text{diss}}^{\text{opt}} \rangle}{\langle P_{\text{diss}}^{\text{c}} \rangle} + 1 \right] \right) \quad (28)$$

2.4.6 Discussion

Illuminating the cantilever with light could induce a temperature increase on the cantilever body. This increase in temperature can reduce the quality factor of the cantilever. A recent study showed that illuminating gold coated cantilever near plasmonic resonance caused a measurable shift in the cantilever stiffness and a decrease in the quality factor⁶⁸. Clearly this effect is not localized, and the temperature of the cantilever body has to increase for the quality factor to decrease. However, to extract nanoscale spectroscopic information of a sample, the opto-mechanical damping must originate and be localized within tip-sample volume of interaction, limited to the effective tip radius. The localization of the observed opto-mechanical damping is evident from Fig. 18 d and f, where the change in A_2 clearly follows the molecular resonance.

The proposed mechanism of PiFM contrast is modeled as optically-mediated damping of the viscoelastic interactions between tip and sample. For example, when the tip

approaches close to the sample, the high electric fields in the optical nanocavity will tend to align the molecules along the axis of the tip. As the tip is retracted from the sample, the molecules will tend to relax back toward their equilibrium position (position without any applied field). These periodic molecular relaxations can occur over a time comparable to the tip oscillation period but with a different phase shift as compared to the tip oscillation phase.

Other possible mechanisms might contribute to the overall opto-mechanical damping. For example, B. N. J. Persson et. al. analyzed the effect of electron-hole (e-h) pair excitation on the life time of a vibrating point dipole near flat metal surface^{69,70}. When a vibrating point dipole located a distance d from semi-infinite metal, inelastic interaction can occur, and part of the interaction energy is radiated away from the system through photon emission and the other part excites e-h pair in the metal, which is a nonradiative loss channel. This lossy interaction quenches the dipole moment of the vibrating molecule. The dipole strength was shown to increase then decrease as a function of d , showing a hump located a few angstroms from metal surface⁷¹. Note that modelling excited molecule with finite-dipole moment instead of point-dipole moment, and replacing flat metal surface with sharp metallic tips, spatially extends near-field gradient of the electromagnetic field, and including these two effects alters the distance dependence of the damping effect and could shift the hump a couple of nanometers away from sample surface.

References

1. Binnig, G., Quate, C. F. & Gerber, Ch. Atomic Force Microscope. *Phys. Rev. Lett.* **56**, 930–933 (1986).
2. Martin, Y., Williams, C. C. & Wickramasinghe, H. K. Atomic force microscope–force mapping and profiling on a sub 100-Å scale. *Journal of Applied Physics* **61**, 4723–4729 (1987).
3. Meyer, G. & Amer, N. M. Novel optical approach to atomic force microscopy. *Appl. Phys. Lett.* **53**, 1045–1047 (1988).
4. Nonnenmacher, M., O'Boyle, M. P. & Wickramasinghe, H. K. Kelvin probe force microscopy. *Appl. Phys. Lett.* **58**, 2921–2923 (1991).
5. Wickramasinghe, H. K. & Williams, C. C. Apertureless near field optical microscope. (1990).
6. Zenhausern, F., O'Boyle, M. P. & Wickramasinghe, H. K. Apertureless near-field optical microscope. *Appl. Phys. Lett.* **65**, 1623–1625 (1994).
7. Magonov, S. N., Elings, V. & Whangbo, M.-H. Phase imaging and stiffness in tapping-mode atomic force microscopy. *Surface Science* **375**, L385–L391 (1997).
8. Schmitz, I., Schreiner, M., Friedbacher, G. & Grasserbauer, M. Phase imaging as an extension to tapping mode AFM for the identification of material properties on humidity-sensitive surfaces. *Applied Surface Science* **115**, 190–198 (1997).
9. Cleveland, J. P., Anczykowski, B., Schmid, A. E. & Elings, V. B. Energy dissipation in tapping-mode atomic force microscopy. *Appl. Phys. Lett.* **72**, 2613–2615 (1998).
10. Voigtländer, B. *Atomic Force Microscopy*. (Springer International Publishing, 2019). doi:10.1007/978-3-030-13654-3.

11. Derjaguin, B. V., Muller, V. M. & Toporov, Yu. P. Effect of contact deformations on the adhesion of particles. *Journal of Colloid and Interface Science* **53**, 314–326 (1975).
12. Johnson, K. L., Kendall, K., Roberts, A. D. & Tabor, D. Surface energy and the contact of elastic solids. *Proceedings of the Royal Society of London. A. Mathematical and Physical Sciences* **324**, 301–313 (1971).
13. Jacobs, T. D. B., Mate, C. M., Turner, K. T. & Carpick, R. W. Understanding the Tip–Sample Contact. in *Scanning Probe Microscopy in Industrial Applications* 15–48 (John Wiley & Sons, Ltd, 2013). doi:10.1002/9781118723111.ch2.
14. Gotsmann, B., Seidel, C., Anczykowski, B. & Fuchs, H. Conservative and dissipative tip-sample interaction forces probed with dynamic AFM. *Phys. Rev. B* **60**, 11051–11061 (1999).
15. Anczykowski, B., Gotsmann, B., Fuchs, H., Cleveland, J. P. & Elings, V. B. How to measure energy dissipation in dynamic mode atomic force microscopy. *Applied Surface Science* **140**, 376–382 (1999).
16. Binnig, G., Rohrer, H., Gerber, Ch. & Weibel, E. Surface Studies by Scanning Tunneling Microscopy. *Phys. Rev. Lett.* **49**, 57–61 (1982).
17. Pohl, D. W., Denk, W. & Lanz, M. Optical stethoscopy: Image recording with resolution $\lambda/20$. *Appl. Phys. Lett.* **44**, 651–653 (1984).
18. Dürig, U., Pohl, D. W. & Rohner, F. Near-field optical-scanning microscopy. *Journal of Applied Physics* **59**, 3318–3327 (1986).
19. Pohl, D. W., Fischer, U. C. & Durig, U. T. Scanning Near-Field Optical Microscopy (SNOM*): Basic Principles And Some Recent Developments. in *Scanning*

- Microscopy Technologies and Applications* vol. 0897 84–90 (International Society for Optics and Photonics, 1988).
20. Wickramasinghe, H. K. & Williams, C. C. Apertureless near field optical microscope. (1990).
 21. Chen, X. *et al.* Modern Scattering-Type Scanning Near-Field Optical Microscopy for Advanced Material Research. *Advanced Materials* **31**, 1804774 (2019).
 22. Lu, F., Jin, M. & Belkin, M. A. Tip-enhanced infrared nanospectroscopy via molecular expansion force detection. *Nature Photonics* **8**, 307–312 (2014).
 23. Wang, L. *et al.* Nanoscale simultaneous chemical and mechanical imaging via peak force infrared microscopy. *Science Advances* **3**, e1700255 (2017).
 24. Rajapaksa, I., Uenal, K. & Wickramasinghe, H. K. Image force microscopy of molecular resonance: A microscope principle. *Appl. Phys. Lett.* **97**, 073121 (2010).
 25. Nowak, D. *et al.* Nanoscale chemical imaging by photoinduced force microscopy. *Science Advances* **2**, e1501571 (2016).
 26. Yang, H. U. & Raschke, M. B. Resonant optical gradient force interaction for nano-imaging and -spectroscopy. *New J. Phys.* **18**, 053042 (2016).
 27. O’Callahan, B. T., Yan, J., Menges, F., Muller, E. A. & Raschke, M. B. Photoinduced Tip–Sample Forces for Chemical Nanoimaging and Spectroscopy. *Nano Lett.* **18**, 5499–5505 (2018).
 28. Ladani, F. T. & Potma, E. O. Dyadic Green’s function formalism for photoinduced forces in tip-sample nanojunctions. *Phys. Rev. B* **95**, 205440 (2017).
 29. Almajhadi, M. & Wickramasinghe, H. K. Contrast and imaging performance in photo induced force microscopy. *Opt. Express, OE* **25**, 26923–26938 (2017).

30. Almajhadi, M. A., Uddin, S. M. A. & Wickramasinghe, H. K. Observation of nanoscale opto-mechanical molecular damping as the origin of spectroscopic contrast in photo induced force microscopy. *Nat Commun* **11**, 5691 (2020).
31. Murdick, R. A. *et al.* Photoinduced force microscopy: A technique for hyperspectral nanochemical mapping. *Jpn. J. Appl. Phys.* **56**, 08LA04 (2017).
32. Jahng, J., Potma, E. O. & Lee, E. S. Tip-Enhanced Thermal Expansion Force for Nanoscale Chemical Imaging and Spectroscopy in Photoinduced Force Microscopy. *Anal. Chem.* **90**, 11054–11061 (2018).
33. Huang, F., Tamma, V. A., Mardy, Z., Burdett, J. & Wickramasinghe, H. K. Imaging Nanoscale Electromagnetic Near-Field Distributions Using Optical Forces. *Scientific Reports* **5**, 10610 (2015).
34. M. Nieto-Vesperinas, P. C. Chaumet & A. Rahmani. Near-field photonic forces. *Philosophical Transactions of the Royal Society of London A: Mathematical, Physical and Engineering Sciences* **362**, 719–737 (2004).
35. Jahng, J. *et al.* Gradient and scattering forces in photoinduced force microscopy. *Phys. Rev. B* **90**, 155417 (2014).
36. Lukas Novotny & Bert Hecht. Principles of Nano-Optics. *Cambridge University Press* <http://www.cambridge.org/us/academic/subjects/physics/optics-optoelectronics-and-photonics/principles-nano-optics-2nd-edition?format=HB&isbn=9781107005464>.
37. Spitzer, W. G., Kleinman, D. & Walsh, D. Infrared Properties of Hexagonal Silicon Carbide. *Phys. Rev.* **113**, 127–132 (1959).
38. Tretinnikov, O. N. IR spectroscopic study of the effect of polymer nanofilm thickness on its surface density. *J Appl Spectrosc* **75**, 64–68 (2008).

39. Zolotarev, V. M., Volchek, B. Z. & Vlasova, E. N. Optical constants of industrial polymers in the IR region. *Opt. Spectrosc.* **101**, 716–723 (2006).
40. Olmon, R. L. *et al.* Optical dielectric function of gold. *Phys. Rev. B* **86**, 235147 (2012).
41. Rakić, A. D., Djurišić, A. B., Elazar, J. M. & Majewski, M. L. Optical properties of metallic films for vertical-cavity optoelectronic devices. *Appl. Opt., AO* **37**, 5271–5283 (1998).
42. Christian Mätzler. MATLAB Functions for Mie Scattering and Absorption, Institut für Angewandte Physik, Research Report No. 2002-08, Bern, Switzerland, 2002.
43. Prodan, E., Radloff, C., Halas, N. J. & Nordlander, P. A Hybridization Model for the Plasmon Response of Complex Nanostructures. *Science* **302**, 419–422 (2003).
44. Östling, D., Apell, P. & Rosén, A. Theory for Collective Resonances of the C 60 Molecule. *EPL* **21**, 539 (1993).
45. Liaw, J.-W., Kuo, M. K. & Liao, C. N. Plasmon Resonances of Spherical and Ellipsoidal Nanoparticles. *Journal of Electromagnetic Waves and Applications* **19**, 1787–1794 (2005).
46. Jian, Z., Xing-chun, D., Jian-jun, L. & Jun-wu, Z. Tuning the number of plasmon band in silver ellipsoidal nanoshell: refractive index sensing based on plasmon blending and splitting. *J Nanopart Res* **13**, 953–958 (2011).
47. Bohn, J. L., Nesbitt, D. J. & Gallagher, A. Field enhancement in apertureless near-field scanning optical microscopy. *J. Opt. Soc. Am. A, JOSAA* **18**, 2998–3006 (2001).

48. Knoll, B. & Keilmann, F. Near-field probing of vibrational absorption for chemical microscopy. *Nature* **399**, 134–137 (1999).
49. Zenhausern, F., Martin, Y. & Wickramasinghe, H. K. Scanning Interferometric Apertureless Microscopy: Optical Imaging at 10 Angstrom Resolution. *Science* **269**, 1083–1085 (1995).
50. Dazzi, A., Glotin, F. & Carminati, R. Theory of infrared nanospectroscopy by photothermal induced resonance. *Journal of Applied Physics* **107**, 124519 (2010).
51. Dazzi, A., Prazeres, R., Glotin, F. & Ortega, J. M. Local infrared microspectroscopy with subwavelength spatial resolution with an atomic force microscope tip used as a photothermal sensor. *Opt. Lett., OL* **30**, 2388–2390 (2005).
52. Wang, L. *et al.* Nanoscale simultaneous chemical and mechanical imaging via peak force infrared microscopy. *Science Advances* **3**, e1700255 (2017).
53. Tumkur, T. *et al.* Wavelength-Dependent Optical Force Imaging of Bimetallic Al–Au Heterodimers. *Nano Lett.* **18**, 2040–2046 (2018).
54. Jahng, J. *et al.* Visualizing surface plasmon polaritons by their gradient force. *Opt. Lett., OL* **40**, 5058–5061 (2015).
55. Zeng, J. *et al.* Sharply Focused Azimuthally Polarized Beams with Magnetic Dominance: Near-Field Characterization at Nanoscale by Photoinduced Force Microscopy. *ACS Photonics* **5**, 390–397 (2018).
56. Tumkur, T. U. *et al.* Photoinduced Force Mapping of Plasmonic Nanostructures. *Nano Lett.* **16**, 7942–7949 (2016).
57. Rajaei, M., Almajhadi, M. A., Zeng, J. & Wickramasinghe, H. K. Near-field nanoprobng using Si tip-Au nanoparticle photoinduced force microscopy with 120:1

- signal-to-noise ratio, sub-6-nm resolution. *Opt. Express, OE* **26**, 26365–26376 (2018).
58. Rajapaksa, I. & Kumar Wickramasinghe, H. Raman spectroscopy and microscopy based on mechanical force detection. *Appl. Phys. Lett.* **99**, 161103 (2011).
59. Tamma, V. A., Beecher, L. M., Shumaker-Parry, J. S. & Wickramasinghe, H. K. Detecting stimulated Raman responses of molecules in plasmonic gap using photon induced forces. *Opt. Express, OE* **26**, 31439–31453 (2018).
60. Tamma, V. A., Huang, F., Nowak, D. & Kumar Wickramasinghe, H. Stimulated Raman spectroscopy and nanoscopy of molecules using near field photon induced forces without resonant electronic enhancement gain. *Appl. Phys. Lett.* **108**, 233107 (2016).
61. Jahng, J. *et al.* Ultrafast pump-probe force microscopy with nanoscale resolution. *Appl. Phys. Lett.* **106**, 083113 (2015).
62. Gu, K. L. *et al.* Nanoscale Domain Imaging of All-Polymer Organic Solar Cells by Photo-Induced Force Microscopy. *ACS Nano* **12**, 1473–1481 (2018).
63. Huang, F., Ananth Tamma, V., Mardy, Z., Burdett, J. & Kumar Wickramasinghe, H. Imaging Nanoscale Electromagnetic Near-Field Distributions Using Optical Forces. *Scientific Reports* **5**, 10610 (2015).
64. Huang, Y. *et al.* Spectroscopic Nanoimaging of All-Semiconductor Plasmonic Gratings Using Photoinduced Force and Scattering Type Nanoscopy. *ACS Photonics* **5**, 4352–4359 (2018).
65. Ladani, F. T. & Potma, E. O. Dyadic Green's function formalism for photoinduced forces in tip-sample nanojunctions. *Phys. Rev. B* **95**, 205440 (2017).

66. Murdick, R. A. *et al.* Photoinduced force microscopy: A technique for hyperspectral nanochemical mapping. *Jpn. J. Appl. Phys.* **56**, 08LA04 (2017).
67. Jin, M. & Belkin, M. A. Infrared Vibrational Spectroscopy of Functionalized Atomic Force Microscope Probes using Resonantly Enhanced Infrared Photoexpansion Nanospectroscopy. *Small Methods* **0**, 1900018.
68. Kim, B. & Potma, E. O. Laser heating of cantilevered tips: Implications for photoinduced force microscopy. *Phys. Rev. B* **100**, 195416 (2019).
69. Persson, B. N. J. & Persson, M. Damping of vibrations in molecules adsorbed on a metal surface. *Surface Science* **97**, 609–624 (1980).
70. Persson, B. N. J. & Lang, N. D. Electron-hole-pair quenching of excited states near a metal. *Phys. Rev. B* **26**, 5409–5415 (1982).
71. Persson, B. N. J. Theory of the damping of excited molecules located above a metal surface. *J. Phys. C: Solid State Phys.* **11**, 4251–4269 (1978).